Summer 2017

Numerical investigation of a plunging airfoil

Matthew James Janechek
University of Iowa

NUMERICAL INVESTIGATION OF A PLUNGING AIRFOIL

by

Matthew James Janechek

A thesis submitted in partial fulfillment of the
requirements for the Master of Science
degree in Mechanical Engineering
in the Graduate College of
The University of Iowa

August 2017

Thesis Supervisor: Associate Professor James H. J. Buchholz

Graduate College
The University of Iowa
Iowa City, Iowa

CERTIFICATE OF APPROVAL

MASTER'S THESIS

This is to certify that the Master's thesis of

Matthew James Janechek

has been approved by the Examining Committee for the thesis requirement for the Master of Science degree in Mechanical Engineering at the August 2017 graduation.

Thesis Committee: _____
James H. J. Buchholz, Thesis Supervisor

_____
H.S. Udaykumar

_____
Casey Harwood

ACKNOWLEDGEMENTS

I would like to thank Professor James Buchholz for allowing me the privilege of carrying out this project. I would also like to thank Professors H.S. Udaykumar and Casey Harwood for their willingness to serve on my committee. Additionally, it would not have been possible to complete this work without the help from the respective members of Professor Buchholz and Professor Udaykumar labs. My sincere thanks to all of you for your willingness to share your vast knowledge. Lastly, I would like to thank my family and friends for their continued support and love. And a special thank you to my wife, Miriam, and daughter, Alice, for keeping me grounded.

ABSTRACT

The goal of this thesis is to investigate vortex dynamics of a plunging airfoil by studying the vorticity transport mechanisms of two-dimensional simulations. Direct numerical simulations were implemented in an effort to provide detailed flow fields that are difficult to capture with experimental methods. The simulations were used to study a simplified flat airfoil in a freestream that was subject to pure plunging motion. Due to computational limits, it was not practical to simulate in three-dimensions and the results are limited to two-dimensions. Quantitative and qualitative analyses were used the validate the two-dimensional simulations and gain insight into the effects of eliminating three-dimensional physics in a nominally two-dimensional flow. Additionally, a parametric study was conducted to analyze the effects of Reynolds and Strouhal numbers on the transport of vorticity.

PUBLIC ABSTRACT

This thesis investigates vortex dynamics of a plunging airfoil by studying the vorticity transport mechanisms of two-dimensional direct numerical simulations. The simulations were used to study a simplified flat airfoil in a freestream that was subject to pure plunging motion. Quantitative and qualitative analyses were used the validate the two-dimensional simulations and gain insight into the effects of eliminating three-dimensional physics in a nominally two-dimensional flow. Additionally, a parametric study was conducted to analyze the effects of Reynolds and Strouhal numbers on the transport of vorticity.

TABLE OF CONTENTS

LIST OF TABLES

Table

LIST OF FIGURES

Figure

NOMENCLATURE

$A = 2h_0$	Peak-to-Peak Plunge Amplitude, m
c	Chord Length, m
$C_L = \frac{2L}{\rho A U_\infty^2}$	Coefficient of Lift
f	Oscillation Frequency, Hz
$f^* = \frac{fc}{U_\infty}$	Non-Dimensional Frequency
Γ	Circulation, m^2/s
h_0	Plunge Amplitude, m
$h_0^* = \frac{h_0}{c}$	Non-Dimensional Plunge Amplitude
$k = \frac{\pi f c}{U_\infty}$	Reduced Frequency
LEV	Leading-Edge Vortex
LHS	Left-Hand Side
ν	Kinematic Viscosity, m^2/s
ω	Vorticity, s^{-1}
OSV	Opposite-Signed Vortex
ϕ	Phase Angle, degrees
PIV	Particle Image Velocimetry
ρ	Density, kg/m^3
$Re_c = \frac{U_\infty c}{\nu}$	Chord-Based Reynolds Number
RHS	Right-Hand Side
$St = \frac{fA}{U_\infty}$	Strouhal Number

u	Velocity, m/s
$u^* = \frac{u}{U_\infty}$	Non-Dimensional Velocity
U_∞	Free-Stream Velocity, m/s

CHAPTER 1
INTRODUCTION

1.1 Motivation

The study of vortex dynamics is a highly complex and active sub-field of fluid mechanics that is relevant to many engineering applications as well as biological motion. Interactions of vortices with surfaces and other vortices produces complex flow patterns and unsteady aerodynamic forces. Impacts of these vortex interactions can be beneficial to an airfoil (e.g. lift generating) or disadvantageous (e.g. inducing flutter). Significant efforts have been made to study these vortex interactions in an effort to understand the correlation between vortex dynamics and airfoil parameters, such as the effects of cross-sectional shape and kinematic motion [11, 30, 12, 13]. Biological creatures that propel themselves through flapping and swimming have been sources of inspiration for many studies characterizing the physical mechanisms of lift and thrust generation [21, 28, 34]. Despite these, and numerous more examples of published research, the underlying physics of vortex dynamics are not completely understood.

Recent research has provided new insight into one area of vortex dynamics, the physics governing the growth and evolution of leading-edge vortices. The work conducted by Wojcik and Buchholz [35] studied the leading-edge vortex (LEV) of a rotating blade, and analysis showed that vortex strength could be perpetually regulated on a vortex stably attached to the blade by vorticity annihilation mechanisms.

The resulting mechanisms were found to be important sources for regulating the stability of an LEV. Similarly, Eslam Panah and Buchholz [7] investigated the LEV and trailing-edge vortex (TEV) developments of a plunging airfoil. This work was advanced in Eslam Panah et al. [22] by analyzing the fluxes of vorticity to quantitatively measure the sources and sinks of vorticity. The results of [22] found that the entrainment of secondary vorticity from the surface of the airfoil was an important mechanism for determining the strength and stability of a LEV. These projects have provided compelling developments into the current understanding of unsteady aerodynamics and form the basis for the work in this thesis.

While the research discussed to this point has predominantly been conducted using experimental methods, several simulations of vortex dynamics have been conducted using numerical methods. For example, Lewin and Haj-Hariri [12] conducted two-dimensional simulations of heaving airfoils to characterize the flow and thrust generation at low Reynolds numbers. Specific to the formation of LEVs, Visbal (2009) [33] implemented large eddy simulations (LES) to study the entrainment of vorticity into an LEV. The results of these, and other, numerical simulations have provided detailed insight into vortex dynamics that would be difficult to fully capture using experimental techniques such as particle image velocimetry (PIV). For example, detailed surface pressures and stress distributions obtained from simulations can help elucidate mechanisms of lift, thrust, and vorticity production. Therefore, numerical simulations will play an important role into the continued research of vortex dynamics.

As with all engineering problems, assessing the assumptions and simplifications of physical phenomena is critical to determining the accuracy of the problem's solution. When implementing numerical simulations with turbulence models, the simulation's solutions are dependent upon the accuracy of the turbulence model representing the true physical nature of the flow. Specifically, for LES simulations, the large eddies in a flow are solved for directly, but a subgrid-scale (SGS) model is used to approximate the small scale structures. For research into the complex interactions of small scale eddies and their effects on LEVs, similar to the work of Eslam Panah et al. [22], SGS models can introduce assumptions that do not necessarily model the physical phenomena, especially for transitional flows such as those associated with biological flapping flight. This is partly due to the fact that the physical phenomena is not well understood. Therefore, for research involving the study of small scale structures in LEV formation, the use of direct numerical simulations (DNS) is desired; where all spatial and temporal scales are solved for without introducing a turbulence model. During the author's literature review, no existing studies were found that performed DNS simulations on LEV formation of a plunging airfoil within the transitional flow regime. The main reason for this lack of research is due to the expensive computational requirements needed to simulate the flow using DNS. Advances in CFD methods have made it possible to implement DNS codes for higher Reynolds number flows; the implementation of adaptive grids, efficient numerical schemes, and parallel processing are some of these advancements. Therefore, a goal of this work was to develop a framework for implementing DNS simulations to further the study of

LEV stability in the transitional regime. Due to the computational expense of these simulations, only two-dimensional simulations were performed. However, since published experimental data are available for the exact same problem (necessarily with fully three-dimensional physics), this work also constitutes a detailed investigation into the role of three-dimensional flow physics on vortex evolution and transport in a nominally two-dimensional flow.

1.2 Literature Review

1.2.1 LEV Importance

LEVs are an active area of interest due to their ubiquity and ability to produce large lift forces. As will be discussed in the following sections, an accumulation of vorticity results in concentrated areas of high kinetic energy that produces low pressure regions along the surface of the airfoil facing the LEV [23]. The resulting low pressure regions induce lift forces not seen in steady aerodynamics. Therefore, advancing the study of unsteady aerodynamics requires a thorough understanding of the formation and evolution of LEVs.

1.2.2 LEV Formation

As previously stated, LEVs form at the leading-edge of an airfoil. But LEVs do not appear spontaneously; initially the region around the airfoil is an attached boundary layer. Due to the induced flow dynamics, e.g. from a plunging or rotating airfoil, an adverse pressure gradient (APG) will develop on the airfoil's surface [5]. When a significantly large APG develops, vorticity will be ejected from the bound-

ary layer which results in the in the roll-up and separation of the boundary layer from the surface [5, 32]. After its initial formation, it is important that an LEV remain connected to the boundary layer through a flux of vorticity from the leading edge's shear layer. This flux of shear layer vorticity acts to increase the circulation of the LEV which results in increased strength and interactions from the LEV with its surrounding surfaces and vortices. Surfaces near the LEV will develop pressure gradients along the surface due to the no-slip condition that results in the generation of opposite-signed vorticity (secondary vorticity) to the LEV [5, 8]. As the motion of the airfoil continues, the LEV will become detached [5, 26]. Recent studies have demonstrated that entrainment of opposite-signed vorticity into LEVs is an important mechanism for detachment [12, 33, 35]. It is further suggested that the entrainment of secondary vorticity is important to gradually annihilating the shear layer vorticity flux [22].

1.2.3 LEV Evolution

After the formation and detachment of an LEV, the vortex still interacts with the airfoil and continues to induce aerodynamic forces. The magnitude of this effect is dependent on the proximity of the LEV to the airfoil's surface [4]. Further studies have been conducted on how to maximize the effects of an LEV, with the overall goal of stabilizing it and offsetting detachment. Jones and Babinsky [9] performed analysis on the dependence of Reynolds number to the formation of an LEV. From their study it was determined that the Reynolds number had little effect on the magnitude of the

detachment circulation and flow structures that resulted in the formation of an LEV. The results of [9] did show that increasing Reynolds numbers between 10,000 and 60,000 of a waving flat wing did effect the rate at which circulation was produced, where an increased Reynolds number resulted in a decreased rate of non-dimensional circulation production, which resulted in an increased duration that the LEV would stay attached. Similarly, Rival et al. [25] varied plunging motions of an airfoil to determine the effects of varying plunging velocity during a cycle. The results of [25] showed that the peak strength of the LEV could be increased by effectively delaying the maximum angle of attack. Furthermore, several studies have shown that the combination of plunging and pitching motions can result in increased performance when compared to a purely plunging airfoil [16, 31]. By combining plunging and pitching motion, the effective angle of attack is changed which appears to be the main parameter governing the evolution of an LEV.

Three-dimensional effects on the formation of a LEV have been a recent area of study. The interest of spanwise transport mechanisms altering the circulation of a LEV stem from the study of delta wings and rotating airfoils. In delta wings, spanwise flow results from the wing's swept nature and contributes to stabilization of an LEV by transporting vorticity from the LEV along the span [15, 24]. Several theories into the stability of LEVs on rotating blades have been hypothesized, including: spanwise flow (similar to transport mechanism of a delta wing) [6], downwash from tip vortices [2, 27], and secondary vorticity annihilating the vorticity of an LEV [35]. As previously stated, the results in [35] indicate that the entrainment of secondary vorticity and the

resulting annihilation of the primary vorticity are the main mechanisms for regulating LEV vorticity. For plunging airfoil, Eslam Panah et al. [22] applied the methods of Wojcik and Buchholz [35] and showed that three-dimensional fluxes of vorticity, on a nominally two-dimensional airfoil, are minimal when compared to the diffusion of vorticity from the airfoil's surface. Therefore, the current research indicates that for a nominally two-dimensional airfoil, three-dimensional effects are minimal and that the stability of a LEV is instead dominated by the transport of vorticity from the leading edge shear layer and the opposite signed vorticity generated as a result of the interactions of the LEV with the airfoil's surface.

1.2.4 Experimental Setup

The work of Eslam Panah et al. [22] and Akkala [1] were used as the sources for defining the simulation domain and kinematics. The experimental setup consisted of a water channel with a test section width of 0.61 m and a water depth of 0.33 m (Figure [22]). An aluminum airfoil with chord length of 76 mm, thickness of 3 mm, and span of 304.8 mm was used in the study to provide a nominally two-dimensional flow. To further limit the flow to two-dimensions, the freestream surface was constrained 0.6 m upstream and downstream of the airfoil by free-surface skimmer plates composed of rigid flat plates. Sinusoidal plunging motion of the airfoil was controlled by a 24 VDC servo motor and Advanced Motion Control amplifier (model BE12A6J) mated to a scotch yoke mechanism. Data collection was performed with two-component digital PIV.

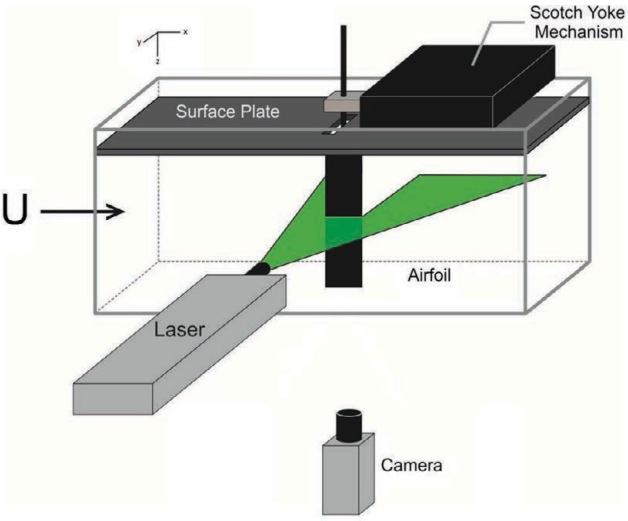

Figure 1.1: Experimental setup for the nominally two-dimensional flow. Adopted from Eslam Panah et al. [22].

1.3 Thesis Objectives and Overview

1.3.1 Objective

As seen in Section 1.1, vortex dynamics are an active field of research. The work of Wojcik and Buchholz [35], Eslam Panah [7], and Akkala [1] have provided a framework for advancing the understanding of vortex dynamics associated with unsteady airfoils. The primary goal of this work is to advance the tools available for analyzing LEV stability and explore the consequences of ignoring three-dimensional effects. Whereas the work of Wojcik, Eslam Panaet, and Akkala were conducted experimentally, this work developed and used a framework for investigating plunging airfoils using DNS simulations. The simulations were validated using the experimental data and the vorticty flux analysis of Eslam Panah et al. [22], which was adapted for

the use with the simulation results. Lastly, a parametric study was conducted using two-dimensional DNS simulations to summarize the effects on the stability of an LEV by varying the Reynolds and Strouhal numbers.

1.3.2 Overview

Chapter 2 provides an introduction to the methods used in studying the plunging airfoil. An overview of the simulation domain is given along with describing the kinematics of the airfoil's motion. A summary of the numerical methods used in the DNS flow solver with moving boundaries is given. Lastly in Chapter 2, an explanation of the the vorticity flux analysis is given along with an explanation for its adaptation to the simulation data.

Chapter 3 describes the simulations' results and discusses the analysis performed on the simulations. Validations were conducted using qualitative comparison of the LEV evolution and quantitative measures of the airfoil forces and analyses of the vorticity fluxes. Last in Chapter 3, the results of the parametric study are discussed. Chapter 4 summarizes this work's findings and discusses future work that would further advance the understanding of LEV stability.

CHAPTER 2
METHODOLOGY

2.1 Domain Definition

The work conducted by Akkala [1] was used for validation and also formed the basis for defining the airfoil dimensions used in the simulations. The experimental airfoil consisted of a flat plate with rounded leading and trailing edges. Figure 2.1 shows the profile of the airfoil. The following dimensions were used for the experimental work: chord length (c) of 76.2 mm and thickness (t) of 3.175 mm.

Figure 2.1: Simplfied airfoil shape.

2.1.1 Simulation Domain

Because the numerical methods of the flow solver work best with values close to unity, the experimental domain was translated into non-dimensional form using the chord length as the characteristic length. Therefore, the non-dimensional simulation chord length (c^*) was equal to unity and the non-dimensional thickness (t^*) was $\frac{3.175}{76.2} \approx 0.0417$.

A rectangular domain (Figure 2.2) was used for the simulations; the airfoil

was positioned sufficiently away from the boundaries so that vortex interactions with the boundaries did not generate misleading results. The non-dimensional length and height dimensions of the domain were 9×6. For the 2D simulations, the free-stream flow went from left to right along the x-axis, while the vertical plunging motion was perpendicular to the free-stream along the y-axis. The inlet was three non-dimensional chord lengths upstream of the airfoil's leading edge and the outlet was five non-dimensional chord lengths downstream of the airfoil's trailing edge. The airfoil chord line was three non-dimensional chord lengths above and below the bottom and top boundaries while the airfoil was stationary.

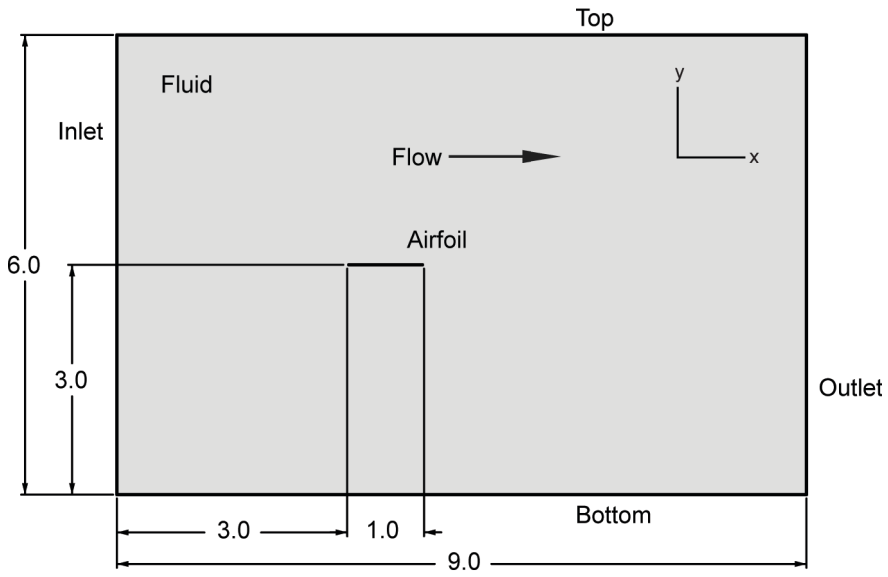

Figure 2.2: Simulation domain, showing the overall dimensions and the placement of the airfoil.

The flow solver uses an adaptive grid, where the mesh is refined every iteration based on the vorticity of the flow field. Initial inputs are given for the grid size and number of grids cells spanning the domain. For the $Re = 10,000$ and $St = 0.3$ case, the initial cell size was 0.008×0.008 in the x and y directions, respectively. Four levels of mesh refinement were allowed for a minimum cell size of 0.001×0.001. Lastly, the duration of the simulations were set so that five full cycles of plunging motion were proceeded by two convective time steps of a stationary airfoil. The stationary airfoil was important for establishing a boundary layer before motion began. Five plunging cycles were selected as a compromise of providing multiple cycles for comparison to identify a nominal steady state and to limit computational run time.

2.1.2 Airfoil Kinematics

The flat airfoil had a prescribed sinusoidal motion in the vertical direction, referenced from the center of the plunging cycle. The displacement, velocity, and acceleration are given by:

$$h = h_0 \sin(2\pi f t) \tag{2.1}$$

$$\dot{h} = 2\pi f h_0 \cos(2\pi f t) \tag{2.2}$$

$$\ddot{h} = -(2\pi f)^2 h_0 \sin(2\pi f t) \tag{2.3}$$

With the following independent variables: h_0 as the motion amplitude in meters, f as the motion frequency in Hertz, and t as the time in seconds. Note that, the motion prescribed in Akkala [1] differs by a factor of -1, where the plate motion moves downward initially instead of upward as seen in the simulations. To compensate for

the difference, the simulation results were adjusted by shifting the associated phase by $-180°$, resulting in the simulation data being presented in a consistent manner with the experimental data.

2.1.3 Non-Dimensional Airfoil Kinematics

As stated previously, the simulations were executed in a non-dimensional form and use the chord length and the free-stream velocity as the characteristic length and characteristic velocity, respectively. Using these parameters the variables in Equations 2.1-2.3 can be transformed into non-dimensional form as follows:

$$h_0^* = \frac{h_0}{c} \tag{2.4}$$

$$f^* = \frac{fU_\infty}{c} \tag{2.5}$$

$$t^* = \frac{tc}{U_\infty} \tag{2.6}$$

Note that the non-dimensional forms of the variable are designated with a superscript *. Using Equations 2.4, 2.5, and 2.6, the equations of motion (Equations 2.1, 2.2, and 2.3) can be transformed into the non-dimensional displacement, velocity, and acceleration of the plate, as follows:

$$h^* = \frac{h_0}{c}\sin\left(2\pi\frac{fU_\infty}{c}\frac{tc}{U_\infty}\right) = h_0^*\sin(2\pi f^* t^*) \tag{2.7}$$

$$\dot{h}^* = 2\pi\frac{fc}{U_\infty}\frac{h_0}{c}\cos\left(2\pi\frac{fU_\infty}{c}\frac{tc}{U_\infty}\right) = 2\pi f^* h_0^*\cos(2\pi f^* t^*) \tag{2.8}$$

$$\ddot{h}^* = -\left(2\pi\frac{fc}{U_\infty}\right)^2\frac{h_0}{c}\sin\left(2\pi\frac{fU_\infty}{c}\frac{tc}{U_\infty}\right) = -(2\pi f^*)^2 h_0^*\sin(2\pi f^* t^*) \tag{2.9}$$

Equations 2.7, 2.8, and 2.9 are used to characterize the airfoil's plunging kinematics during the simulations. As will be discussed in Section 2.2, these equations will be used to update the airfoil level set for simulating the fluid-solid interaction.

2.1.4 Ramp Function

As stated in Section 2.1.3, the plunging motion was delayed two convective time steps to allow for an adequate boundary layer to develop on the top and bottom surfaces of the airfoil. Additionally, a ramp function was used to limit the plunging amplitude during the first cycle of motion to avoid an impulsive start. The resulting amplitude is given by:

$$\bar{h_0^*} = h_0^* \left(1 - \exp\left(\frac{-4.6}{t_{99\%}} t^*\right)\right) \tag{2.10}$$

Equation 2.10 limits the amplitude (h_0^*) of the sinusoidal motion in Equations 2.7, 2.8, and 2.9 and then continuously ramps up the output amplitude ($\bar{h_0^*}$). At $t^* = t_{99\%}$, $\bar{h_0^*}$ will be 99% of h_0^* and will continue to approach the asymptote h_0^* for $t^* > t_{99\%}$. For the simulations conducted, $t_{99\%} = \frac{PlungingPeriod}{4}$ so that by the time the airfoil reached the top of the periodic motion, the amplitude was at 99% of a normal cycle. Therefore, the simulations implemented versions of Equations 2.7, 2.8, and 2.9 by substituting h_0^* with $\bar{h_0^*}$ given in 2.10.

2.2 Numerical Implementation

The research code pELAFINT3D was used to perform the numerical simulations [20, 18]. The code contains DNS compressible and incompressible flow solvers for moving boundary problems. While the numerical methods implemented within

pELAFINT3D are not the emphasis of this thesis, a brief overview of the numerical methods implemented in pELAFINT3D are given in the following subsections.

2.2.1 Airfoil Boundary Treatment

The flow solver is based on the Cartesian grid method where the governing equations are solved on a Cartesian mesh. For moving boundary problems, the Cartesian grid method inherently solves the governing equations from a Eulerian perspective as opposed to a Lagrangian perspective where the mesh would deform with the motion of the object. Instead, the Cartesian grid method updates the position of the object accordingly and then identifies different types of mesh nodes. Depending on the type of node, the flow solver will appropriately solve, apply boundary conditions, or ignore the nodes. At each timestep the node identification is updated based on the object position.

The boundary of the object in pELAFINT3D is represented using the level set method and solution nodes are identified based on the level set contours. The level set is governed by the level set advection equation, Equation 2.11, where Φ is the level set field and $\vec{V}$ is the propagation velocity of the level set field:

$$\frac{\partial \Phi}{\partial t} + \vec{V} \cdot \nabla \Phi = 0 \tag{2.11}$$

Furthermore, the object's surface is represented as the zeroth level set contour and the sign convention used within pELAFINT3D has positive values representing contours outside the object and negative values representing contours inside the object.

Extrapolation stencils used with the Ghost Fluid Method (GFM) identify fluid,

hybrid, ghost, and fresh nodes at each timestep based on the level set field (Figure 2.3). Fluid nodes fill the domain away from the object boundary. Ghost nodes are immediately inside the object's surface and are used to impose the boundary conditions at the object's surface. Fresh nodes are nodes in a moving boundary problem that have recently transitioned from being a ghost node inside the object to becoming fluid nodes that need to be solved for. Therefore, fresh nodes are identified by a transition from negative to positive level set values. Lastly, hybrid nodes are close to the object's surface and have a positive level set value. Special treatment is applied to the hybrid nodes which represent a buffer between fluid and ghost nodes. Hybrid nodes are determined by a predetermined distance threshold [17]. Once the level set field and nodes have been updated, the fluid and hybrid nodes are solved using a four-step fractional step algorithm. Because the fresh nodes are transitioning from ghost nodes, they do not contain valid flow properties. To compensate for this lack of data, interpolation from the surrounding fluid nodes is required and give fresh nodes approximate values based on the previous timestep's results. As fresh nodes become hybrid nodes in the subsequent timesteps, the nodes are solved for directly but fluctuations can occur in the node data close to the interface due to the initial approximated results of the interpolation. This can ultimately lead to temporal oscillations of the pressures and velocities and is a known numerical artifact of SIM and GFM methods, as demonstrated by Luo 2012 [14]. Higher order interpolation methods can help reduce the oscillations but any large amplitude motion at the boundary will be difficult to accurately approximate.

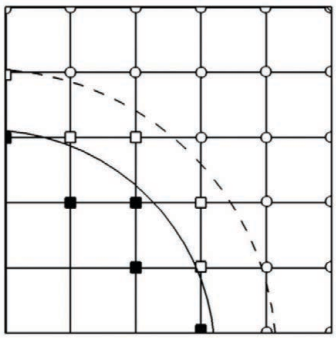

Figure 2.3: The grid node classification of the pELAFINT3D sharp interface technique. Ghost and hybrid nodes are represented by filled and open square symbols while fluid nodes are shown as open circles. The solid line represents the object's surface and the dashed line represents the threshold boundary for defining hybrid nodes. Adopted from [18].

2.2.2 Non-Dimensional Governing Equations

The problem domain was setup in non-dimensional form using characteristic parameters that resulted in a chord length and free stream velocity of unity. Normalizing the length and velocity scales aid the numerical methods used by the flow solver. Additionally, this enables the user to specify the desired Reynolds numbers through the pseudo kinematic viscosity. Therefore, the incompressible Navier Stokes Equations are solved in a non-dimensional form by the flow solver. Equations 2.12 and 2.13 are the non-dimensional versions of the incompressible governing equations:

$$\nabla \cdot \vec{u^*} = 0 \tag{2.12}$$

$$\frac{\partial \vec{u^*}}{\partial t} + \vec{u^*} \cdot \nabla \vec{u^*} = -\nabla p^* + \frac{1}{Re} \nabla^2 \vec{u^*} \tag{2.13}$$

Equations 2.12 and 2.13 are solved for by the flow solver at the fluid and hybrid nodes. A four-step fractional step method is used by the solver to decouple the flow velocity and pressure variables on a collocated cell-centered grid. Step one computes a temporary velocity using a second-order explicit Adams-Bashforth scheme for the time-discretization and a second-order semi-implicit Crank-Nicholson method for the diffusion term. At this step, the continuity equation is not explicitly enforced. Step two eliminates an estimated pressure used in step one which can cause unstable results due to the collocated grid. Steps three and four solve for the next timestep's velocity and pressure and impose the incompressiblity condition by solving a pressure Poisson equation for a divergence-free flow.

Spatial discretization is achieved using second-order finite differences. Fluid boundary nodes use the appropriate forward or backward differencing schemes and non-boundary fluid and hybrid nodes use central differencing. Ghost nodes are used in the discretization to impose interface conditions and require special care. Extrapolation functions are used to probe the interface close to the node and then use a weighted least-squares method of the surrounding nodes to establish an interpolated value for the ghost node. Additional information on pELAFINT3D can be found in the work of Mousel (2012) [20] and Mohaghegh (2017) [19].

2.2.3 Boundary Conditions

As with all numerical simulations, it was necessary to prescribe the boundary conditions used in the solution process. Velocities at the boundaries of the domain

were prescribed with Dirichlet conditions at the inlet, top, and bottom boundaries which established a free-stream velocity of unity in the x-direction. The outlet had a prescribed Neumann condition of zero velocity. Pressures along all domain boundaries were prescribed with a Dirichlet condition of zero. As stated in Section 2.2.1, the airfoil object had boundary conditions imposed at the zeroth level set contour using the ghost nodes which resulted in the desired no-slip condition.

2.3 Flux Analysis

As detailed in Section 2.4, a quantitative vorticity flux analysis was performed on a control region positioned along the top surface of the airfoil. Figure 2.4 displays the 2D rectangular control region A_z where boundaries s_1, s_2, and s_3 extend into the flow field while s_4 is coincidental with the plate surface. The vorticity flux analysis utilized by Eslam Panah et al. [22] was adapted for the simulation data. This flux analysis was used to quantify the sources and sinks of vorticity on the the top surface of the airfoil as it cycled through the plunging motion. A summary of the adaptation of the vorticity flux analysis is given in Section 2.3.1.

2.3.1 Flux Analysis Adaptation

The three-dimensional form of the vorticity flux analysis from [22] is shown below:

$$\frac{\partial \Gamma}{\partial t} = -\int_{A_z} u_z \frac{\partial \omega_z}{\partial z}\, dA_z + \int_{A_z} (\omega_x \frac{\partial u_x}{\partial x} + \omega_y \frac{\partial u_z}{\partial y})\, dA_z - \oint_s \omega_z (\vec{u} \cdot \hat{n})\, ds + \frac{1}{\rho} \int_{s_4} \frac{\partial p}{\partial x}\, ds_4 \quad (2.14)$$

The LHS is the time rate of change of circulation within the control region and should be equal to the sum of the vorticity fluxes on the RHS. The first term on the RHS

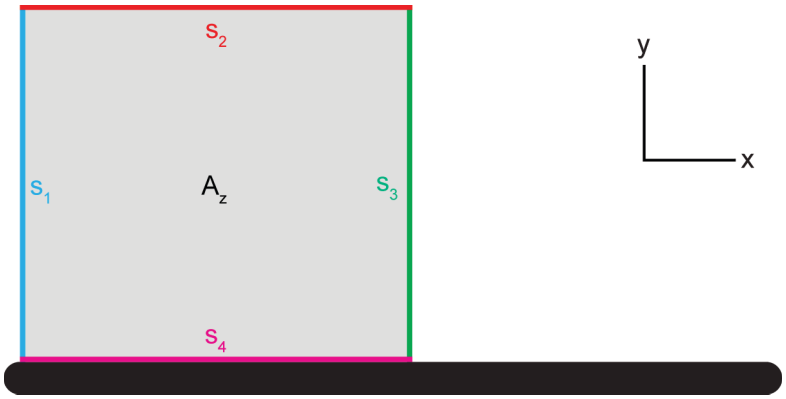

Figure 2.4: Control region for the vorticity flux analysis.

represents the span-wise convective flux along the z-direction. Tilting of vorticity into the in-plane control region is represented by the second term on the RHS. Convection of vorticity into the control region is represented by the third term on the RHS. Because $\hat{n}$ points outward from the control region boundary, a positive value for the integral represents positive vorticity leaving the control region; therefore, a negative sign is needed for the term to show positive vorticity entering the control region as a positive value. Due to the no-flux condition at the airfoil's surface, there is no convective flux of vorticity through the s_4 boundary. Instead, the last term on the RHS represents the diffusion of positive vorticity from the airfoil's surface. The final form of this term was derived to allow experimental pressure measurements along the airfoil's surface which were used to calculate the pressure gradient. Note that vorticity diffusion from boundaries s_1, s_2, and s_3 have been neglected. This assumption has been justified by the experimental data where Equation 2.14 has been shown to be closed within the bounds of experimental error.

For the simulation vorticity flux analysis, Equation 2.14 can be simplified due to the absence of three-dimensional effects. Derivation of the simulation vorticity flux equation can be found in the Appendix, the final form is shown here:

$$\frac{\partial \Gamma_z}{\partial t} = -\oint_s \omega_z(\vec{u}\cdot\hat{n})\,ds + \frac{1}{\rho}\int_{s_4}\frac{\partial p}{\partial x}\,ds_4 \tag{2.15}$$

Comparing Equations 2.14 and 2.15, it is apparent that the fluxes from spanwise convection and out-of-plane tilting are absent in the simulation analysis. This is consistent with the simulations' lack of data in the z-direction which provide the basis any three-dimensional vorticity transport mechanisms.

In summary, the terms of the two-dimensional vorticity flux analysis, Equation 2.15, are as follows. The LHS represents the time rate of change of circulation within the control region. The first term on the RHS represents the convection of vorticity through the control region boundaries s_1, s_2, and s_3. The last term on the LHS represents the diffusion of vorticity along the airfoils surface. Taking the sum of the convective and diffusive fluxes of vorticity along the respective control region boundaries, represents the total fluxes of vorticity for the two-dimensional simulations. As stated previously, the LHS and RHS should be equal if all the vorticity fluxes are properly accounted for.

The control region used for Equation 2.15 is defined in Figure 2.5, where the left boundary (s_1) is 0.021 non-dimensional units from the leading edge, the top boundary (s_2) is 0.459 non-dimensional units from the airfoil's top surface, the right boundary (s_3) is 0.504 non-dimensional units from the leading edge, and the bottom boundary (s_4) coincides with the airfoil's surface.

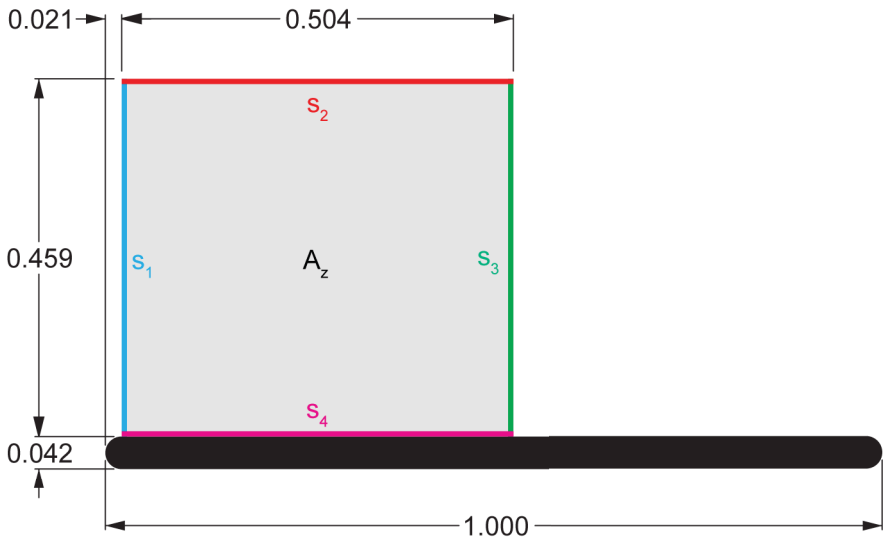

Figure 2.5: Defined control region used for the vorticity flux analysis.

Numerical methods were implemented to compute the fluxes in Equation 2.15. The spatial derivatives in the vorticity and diffusive flux terms were calculated using a second-order finite difference scheme. To provide consistency with the experimental analysis of [1], the simulation results were interpolated onto a uniform grid with a consistent grid spacing. Central differencing was then implemented on the interpolated results. Discetization of the time derivative of circulation on the LHS of Equation 2.15 was also implemented using finite difference. Circulation was calculated by summing the product of z-vorticity and cell area at each discrete node. The time-rate of change in circulation was calculated as a second-order central difference where the circulation difference at the previous and post timesteps were divided by twice the output timestep size.

2.4 Project Scope

The methods presented in this chapter were implemented with the goal of establishing a computational framework for investigating vortex dynamics of a plunging airfoil. DNS simulations were used to study a simplified flat airfoil in a freestream that was subject to pure plunging motion. Due to computational limitations in establishing the framework, it was not feasible to simulate in three-dimensions and therefore the results are limited to two-dimensions. Results were qualitatively and quantitatively analyzed to determine the validity of the two-dimensional simulations by studying the vorticity transport mechanisms. Validation of the simulations was conducted by comparing the results to experimental data, identifying sources of numerical artifacts, and analyzing the short-comings of excluding three-dimensional physics in the vortex generation of a nominally two-dimensional flow. Once the two-dimensional computational framework was validated and characterized, a parametric study was conducted to analysis the effects of Reynolds number and Strouhal number on the formation of a LEV.

Experimental measurements conducted by Akkala [1] were used in the validation of the simulation results. First, a comparison of the lift and drag forces was conducted to validate that the aerodynamics forces were being reasonably captured in the simulations. Once the forces were established, a qualitative analysis was conducted to visually compare the LEV evolution and to develop a sense for the underlying physics in the two-dimensional simulations. Lastly, the vorticity flux analysis used by Akkala was adapted to the simulation data to characterize the two-dimensional

vorticity transport mechanisms.

CHAPTER 3
RESULTS AND ANALYSIS

3.1 Force Comparison

Validation of the simulations was first conducted by comparing the lift and drag forces between the simulation and experimental data at $Re = 10,000$ and $St = 0.3$. Akkala's experimental data [1] implemented a six-axis force transducer at the end of the plunging airfoil to record force data during the plunging cycles. The simulations recorded aerodynamic forces on the airfoil by integrating the fluid pressure and viscous stresses along the airfoil's surface at each time step. Because the simulations were non-dimensionalized, it was not possible to compare the simulation flow fields and forces with the experiments directly. Therefore, the simulation force output and the experimental transducer outputs were transformed into the non-dimensional lift and drag coefficients for comparison.

3.1.1 Filtering and Phase Averaging Simulation Data

The Ghost Fluid Method (GFM) described in Chapter 2 introduces high frequency oscillations in the pressure and velocity solutions at the interface of a moving boundary. Fortunately for the simulation data studied in this thesis, the fluctuating airfoil forces could be accurately filtered before being compared to the experimental data.

Filtering of the force data was achieved by applying a second-order Butterworth filter with a normalized cutoff frequency of 0.01. The cutoff frequency was

normalized relative to half the sampling frequency of 18 Hz and resulted in a cutoff frequency of 0.9 Hz. This resulted in a reduction of the high frequency oscillations introduced at the boundary but maintained the overall trend of the data. To avoid any phase shift in the filtered results, the filtering was performed in the forward and backward directions with the MATLAB function filtfilt. Figure 3.1 shows the raw data for the simulation lift coefficient in red and the filtered result in black.

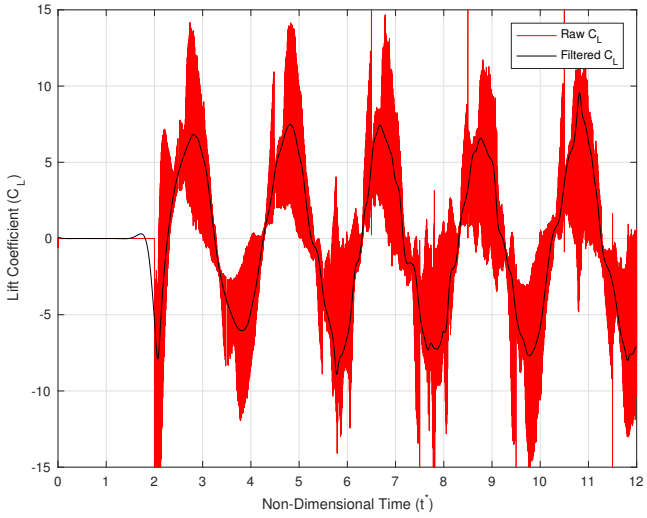

Figure 3.1: Filtered lift coefficient data at Re = 10,000 and St = 0.3.

As can be seen by Figure 3.1, the filtering provided an adequate removal of the high frequency fluctuations with no phase shift but retained cycle to cycle variations. Upon inspection of the transient lift coefficient, the lift appears to become irregular as the simulation progressed. As will be discussed further, the irregular behavior is a

significant deviation from the experimental data and provides insight into the impact of the 2D assumption. Furthermore, because of the chaotic behavior of the vortices, phase averaging is impractical, and only one plunging cycle was be considered for validation purposes. The first cycle of plunging data without the effects of the ramp function (cycle 2) was be used because it does not contain the effects of the ramp function of cycle 1 and exhibits the least chaotic behavior in the vortices. Figure 3.2 shows a closeup of the raw and filtered coefficient of lift data on cycle 2. Similarly, the drag coefficient was filtered to eliminate the oscillations as shown in Figure 3.3.

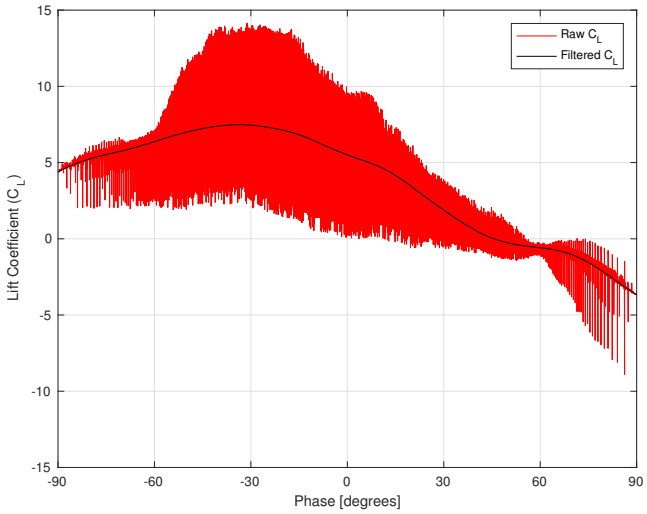

Figure 3.2: Filtered lift coefficient data during the second plunging cycle.

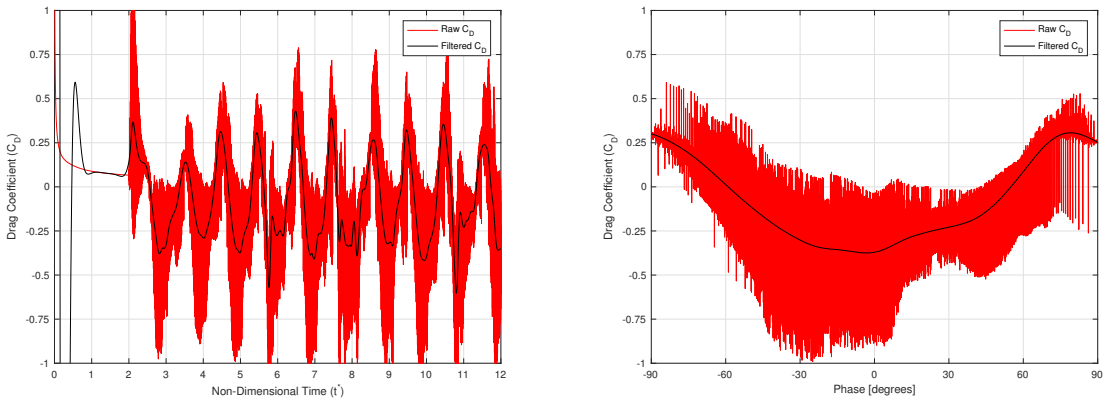

(a) Full Simulation (b) Second plunging cycle

Figure 3.3: Filtering of the simulation drag coefficient.

3.1.2 Comparison of Non-Dimensional Forces

The lift coefficient is defined as:

$$C_L = \frac{2F'_y}{\rho c U_\infty^2} \tag{3.1}$$

Where F'_y, ρ, A, and U_∞ represent the lift force per unit span, density, chord length, and free-stream velocity, respectively. The lift coefficient was used to non-dimensionalize the simulation and experimental lift forces for comparison.

Table 3.1 summarizes the parameters associated with the simulation and experimental data sets used in Equation 3.1.

The filtered forces were compared to the experimental measurements. Figure 3.4 shows the lift coefficient of the simulation (solid line) and experiment (dashed line) during the downstroke of the airfoil's plunging motion. There is a strong similarity between simulation and experimental lift coefficient in both magnitude and phase,

Table 3.1: Experimental and simulation parameters.

Parameter	Experimental	Simulation
Chord (c) $[m]$	76e-3	1
Span (S) $[m]$	3.048e-1	-
Area (A) $[m^2]$	0.232	-
Density (ρ) $[\frac{kg}{m^3}]$	1,000	1
Velocity (U_∞) $[\frac{m}{s}]$	0.132	1
Frequency (f) $[Hz]$	0.865	0.5
Plunge Amplitude (h_0) $[m]$	2.29e-2	0.3

suggesting that the 2D assumption does not effect the lift generating mechanisms.

Similarly, the drag coefficient was compared between the simulation and experimental data for validation. The drag coefficient is defined as:

$$C_D = \frac{2F'_x}{\rho c U_\infty^2} \tag{3.2}$$

Figure 3.5 shows the drag coefficient for the simulation and experimental data as solid and dashed lines, respectively. Again, there is similarity between the two data sets but in this case the simulation results do deviate from the experimental data at the end of the downstroke. This may be the result of the physical difficulties in accurately measuring drag on a flat plate, which has a much smaller magnitude force when compared to the lift under these circumstances. But overall, there is excellent agreement between the two data sets and again suggests that the 2D assumption does not affect the drag mechanisms.

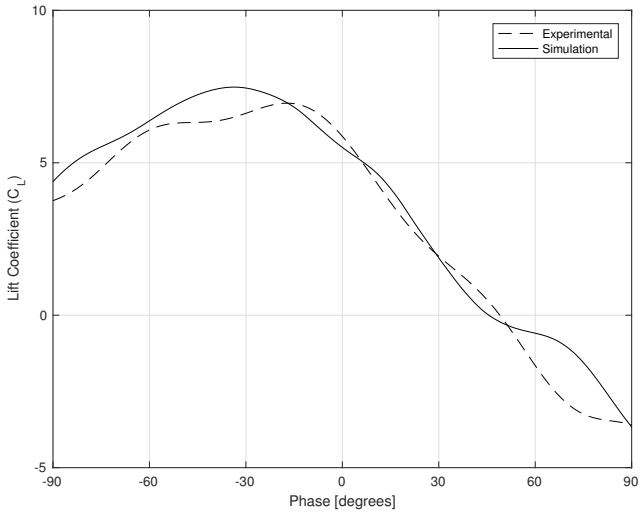

Figure 3.4: Lift coefficient comparison between the experimental and simulation data, at $Re = 10,000$, $St = 0.3$, $k = 1.57$, and $\frac{h_0}{c} = 0.3$.

3.2 Vortex Evolution

Qualitative vortex evolution comparisons were made between the simulation and experiment by overlaying the experimental vorticity results of Akkala [1] with the simulation vorticity results at $Re = 10,000$ and $St = 0.3$. Figure 3.6 displays the formation of the LEV at every ten degrees of plate motion during the downstroke where the saturated colored vorticity contours represent the simulation vortex dynamics and the outlined faint colored vorticity contours represent the experimental vortices. In each case, blue contours represent negative vorticity and red contours represent positive vorticity. The PIV measurements did not capture the flow below the airfoil and the experimental vorticity contours are phase averaged over 100 cycles. The simulation vorticity contours are representative of a single cycle (cycle 2) of the

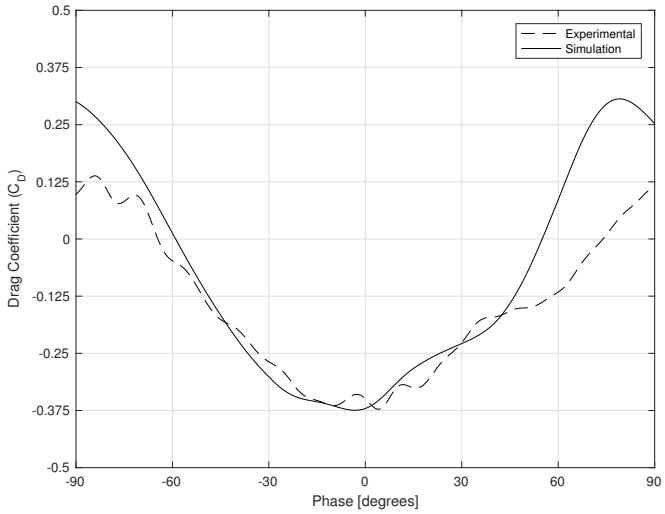

Figure 3.5: Drag coefficient comparison between the experimental and simulation data.

simulation results.

Focusing only on the development of the LEV, Figure 3.6 demonstrates that the vortex growth and position correspond well between the simulation and experimental results. At 0° the LEV has developed a significant region of secondary vorticity along the plate surface which can be seen in both data sets. Between 50° and 70° the LEV appears to separate, and both the simulation and experimental results show the LEV being cutoff from the shear layer by the eruption of secondary vorticity [5]. Additionally, both data sets show that the negative vorticity of the LEV appears to entrain some positive vorticity during these phases. Overall, qualitatively the LEV evolution between the experimental data and simulation cycle 2 data are in good agreement. As previously noted, the simulation vortices became increasingly chaotic

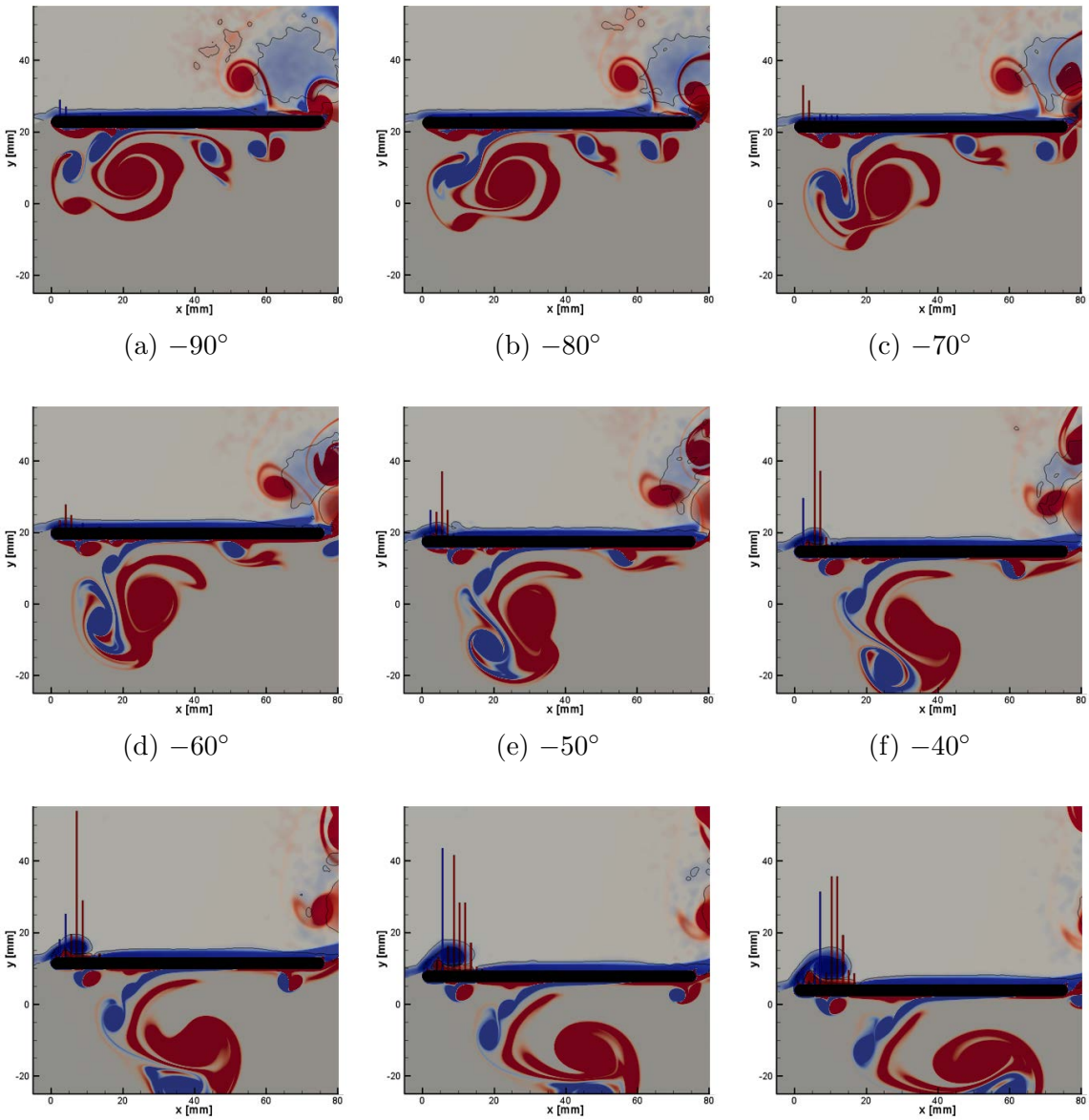

(a) −90° (b) −80° (c) −70°

(d) −60° (e) −50° (f) −40°

(g) −30° (h) −20° (i) −10°

Figure 3.6: Re=10,000 vortex evolution overlay of experimental and simulation data.

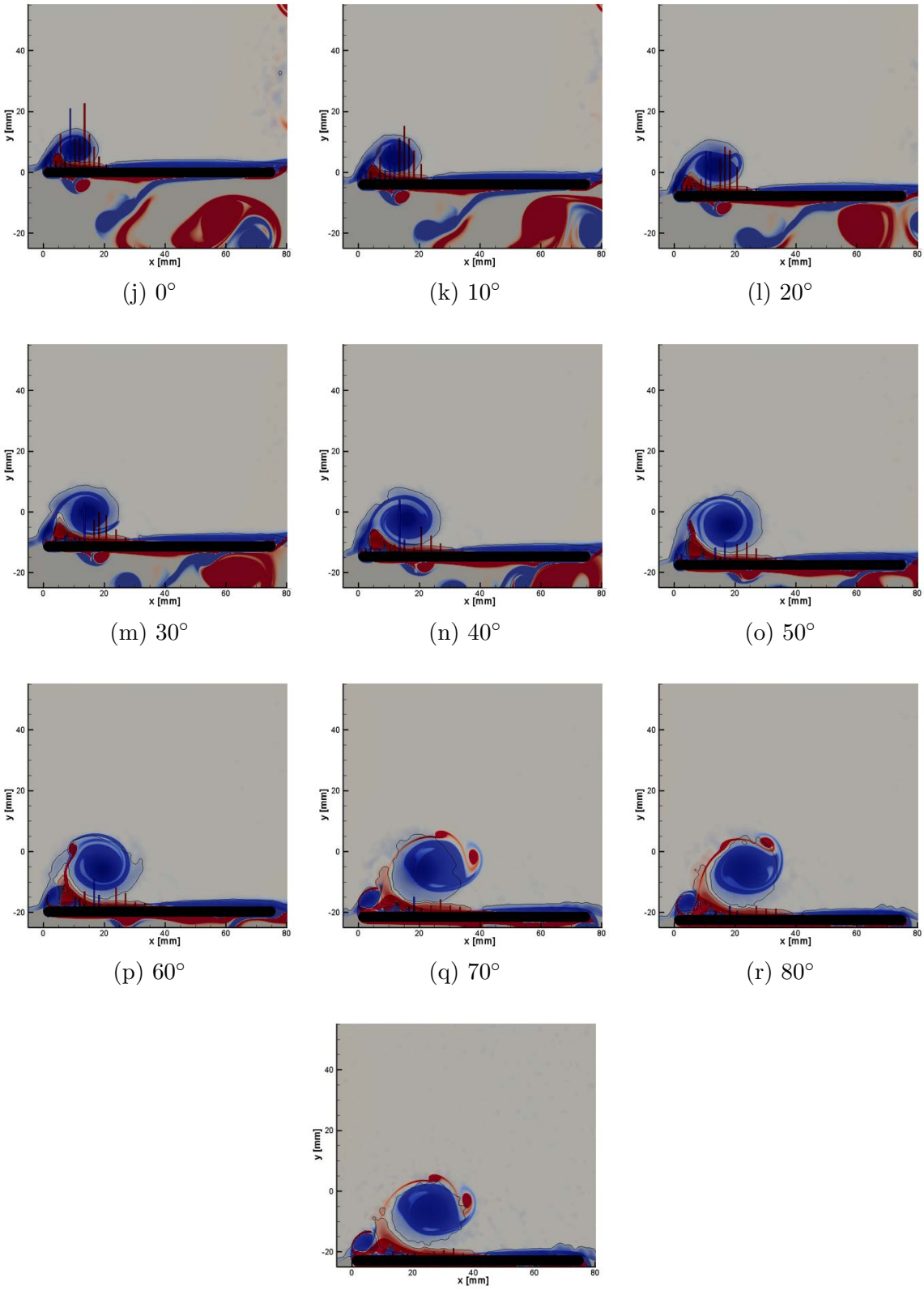

(j) 0° (k) 10° (l) 20°

(m) 30° (n) 40° (o) 50°

(p) 60° (q) 70° (r) 80°

(s) 90°

Figure 3.6: Re=10,000 vortex evolution overlay of experimental and simulation data with a vertical plunging motion and a freestream flow from left to right.

with each additional plunging cycle so the agreement between experimental and simulation LEV evolution diminishes with each cycle of the simulation. This suggests that the 2D assumption begins to affect the LEV formation after multiple plunging cycles when the previous cycles' LEVs have not seen significant breakdown or convected downstream.

3.3 Vorticity Flux Analysis

A detailed quantitative analysis was conducted to characterize the sources and sinks of vorticity in a moving control region on the top side of the plate using the methods outlined in Chapter 2. The two-dimensional vorticity flux analysis isolates the convective fluxes through each boundary of the control region defined in 2.1.1, including the leading edge shear layer, the convective flux through the top of the control region (s_2), the convective flux through the downstream edge (s_3), and the diffusive flux from the airfoil surface. For the Re=10,000 and St=0.3 simulation, s_2 was placed significantly above the airfoil's surface where it would be expected that minimal convective flux would occur through this boundary. Furthermore, s_3 was located slightly past the mid point along the airfoil's chord, for a LEV that does not quickly detach and convect downstream it was expected that only small quantities of vorticity would pass through this edge. Therefore, the dominant sources and sinks of vorticity would be characterized by the shear layer and diffusive fluxes.

Figure 3.7 displays the initial vorticity flux analysis of one downstroke cycle. The vorticity flux analysis should show that the time rate of change of circulation

equals the sum of the vorticity fluxes. In Figure 3.7, the summed vorticity fluxes are shown in dark blue and the time rate of change of circulation is shown in black. Overall, the trend of the fluxes are similar but there are oscillations in the summed vorticity fluxes caused by the GFM. Looking at the two main sources and sinks of vorticity, the diffusive flux shown in light blue and shear layer flux shown in purple, it can be seen that the diffusive flux exhibits increasing oscillations around 0°. To overcome these numerical artifacts, the diffusive flux and shear layer flux were filtered using forward and reverse second-order Butterworth MATLAB filter filtfilt, with a normalized cutoff frequency of 0.01. Again, the cutoff frequency was normalized relative to half the sampling frequencies. Because the flow data was recorded at every ten degrees of the plate's motion, the sampling frequency was much lower than that of the force data which was recorded at every time step. The lower sampling frequency resulted in filtering that does not as accurately capture the true nature of the flux. Regardless, the filtering does provide an improvement and the resulting filtered sum of the vorticity fluxes is in better agreement with the time rate of change of circulation. For the remainder of this thesis, all vorticity flux analysis results will be displayed as the filtered diffusive, shear layer, and total fluxes only.

As previously stated, five cycles of plunging motion were simulated where the first cycle contained a ramp function to avoid an impulsive start. The flux analysis was performed on the last four cycles (cycles 2-5) but not cycle 1 to avoid analyzing any effects introduced by the ramp function. Figure 3.8 displays the vorticity flux analysis for the last four cycles (cycles 2 through 5) during the cycles plunging downstroke.

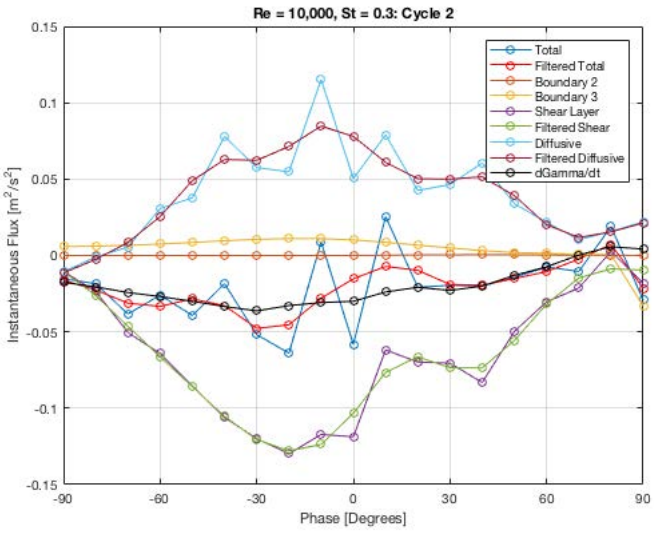

Figure 3.7: Vorticity flux analysis filtered and unfiltered data, at $Re = 10,000$, $St = 0.3$, $k = 1.57$, and $\frac{h_0}{c} = 0.3$.

It is apparent that not all cycles exhibited the same flux behavior. Cycles 2 and 3 show similar trends, where cycle 4 shows weakened diffusive and shear layer fluxes, and cycle 5 shows a spike in the shear layer flux around $-30°$.

The differences seen in the vorticity flux analysis between plunging cycles can be attributed to an increased chaotic behavior of the vortices as the flow evolves and vortex interactions increase. While it was seen in Section 3.2 that the vortex evolution of the LEV compared well between the phase averaged experimental data and cycle 2 of the simulation data, Figure 3.8d shows the deviation of LEV formation and the effects of chaotic vortex interactions. It is hypothesized that these increased vortex interactions are are the result of the LEVs not sufficiently breaking down after their formation. The lack of vortex breakdown could be attributed to the lack of vorticity

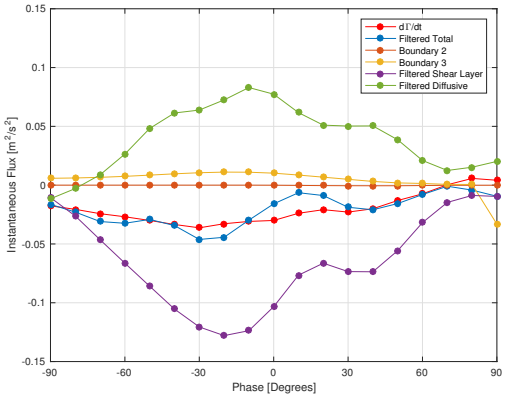

(a) Cycle 2

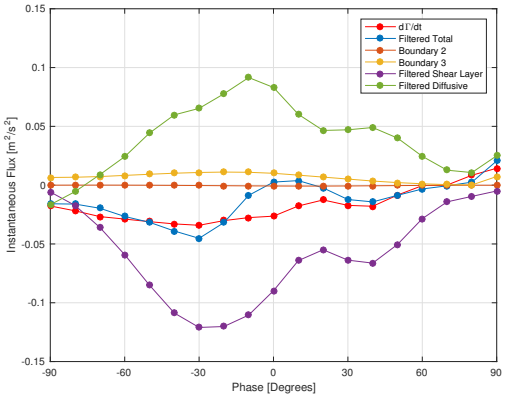

(b) Cycle 3

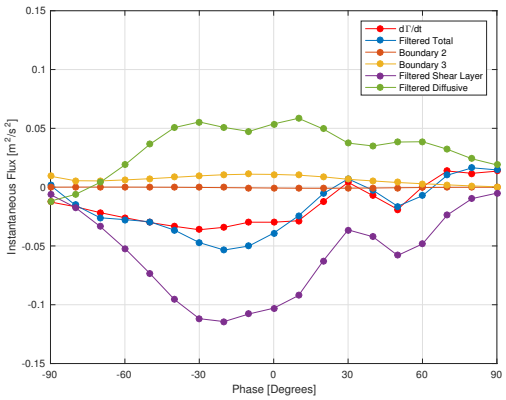

(c) Cycle 4

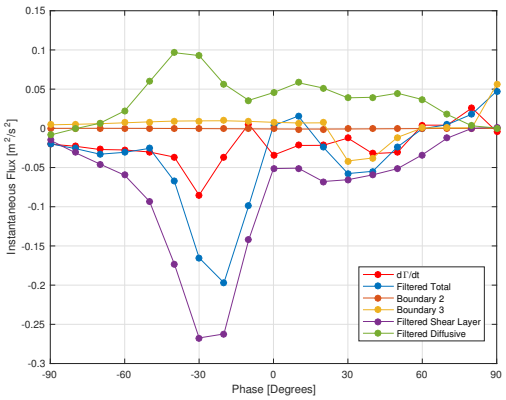

(d) Cycle 5

Figure 3.8: Vorticity flux analysis for Re = 10,000 and St = 0.3.

sinks in the absence of three-dimensional effects. As presented in Chapter 1, prominent three-dimensional effects of a LEV have been observed in the form of axial flow and vortex stretching. The two-dimensional simulations lack these mechanisms and it is hypothesized that these mechanism are necessary for modeling vortex breakdown.

Figure 3.9 shows the phase-averaged experimental flux analysis performed by Akkala and can be compared to Figure 3.8. It is seen that the simulation flux analyses in Figures 3.8a and 3.8b are in good phase and magnitude agreement with the respective fluxes in the experimental analysis of Figure 3.9. Therefore, the hypothesis of three-dimensional mechanisms needed in the breakdown of vortices is consistent with the results of the two-dimensional simulations. When there is an absence of extraneous vortex interaction, the formation of an LEV correlates well with experimental data. But the absence of vortex interaction during LEV formation is not sustainable in a two-dimensional simulation and more frequent vortex interactions occur and become increasingly complex with repeated plunging cycles. This hypothesis is supported by the analyses of the forces and vortex evolution used for validation, where cycle 2 of the simulation data correlated well with the experimental data but additional cycles began to show deviations. In summary, this work indicates that the LEV formation is not highly dependent upon three-dimensional mechanisms but that the breakdown of the LEV, after separation, is dependent upon three-dimensional mechanisms.

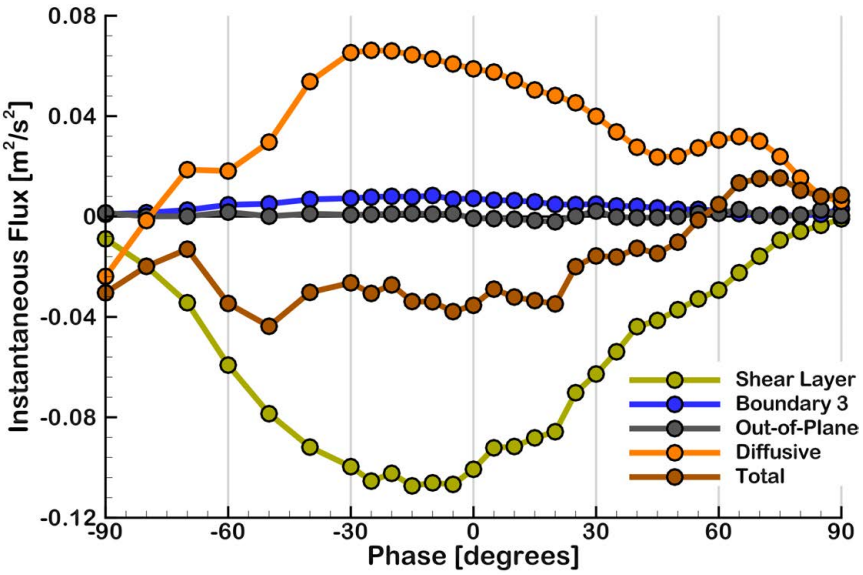

Figure 3.9: Experimental vorticity flux analysis filtered. Adopted from Akkala [1].

3.4 Parametric Study

The discussion to this point has been specific to one simulation case, where $Re = 10,000$ and $St = 0.3$. As stated in Chapter 1, these parameters were specified for their significance to biological motion and for comparison with the available experimental data. In this section, the results of simulations in a parametric study, with varying Reynolds number and Strouhal number, are investigated through the analyses of aerodynamic forces, LEV vortex evolution, and the fluxes of vorticity during LEV formation. Table 3.2 summarizes the flow variables used in the parametric study, where three Reynolds numbers and three Strouhal numbers were varied to investigate the effects they had on the flow dynamics.

Table 3.2: Parametric study parameters.

$Case$	St	Re_c	U_∞^*	c^*	h_0^*	f^*
1	0.3	1,000	1.0	1.0	0.3	0.5
2	0.2	5,000	1.0	1.0	0.3	0.333
3	0.3	5,000	1.0	1.0	0.3	0.5
4	0.4	5,000	1.0	1.0	0.3	0.667
5	0.3	10,000	1.0	1.0	0.3	0.5

3.4.1 Parametric Study: Forces Comparison

To begin, lift and drag coefficients were compared for the cases outlined in Table 3.2. Similar methods to those in Section 3.1 were used to generate the filtered data shown in Figure 3.10. Case 3, with a $Re = 5,000$ and $St = 0.3$, is shown by a dash-dot line and is presented as the median case for the parametric study. From Figure 3.10, the varied Strouhal number cases are represented as dashed lines and the varied Reynolds number cases are represented as solid lines. The figure shows that varying the Strouhal number provides the greatest changes in lift generation. For the three cases with a consistent Strouhal number but a varying Reynolds number, very little variation was seen in the lift coefficient. For the three varying Strouhal numbers, there is a proportional relationship. The increasing lift coefficient can be attributed to the increased dynamic pressure at the higher Strouhal numbers. Similarly, Figure 3.11 shows the results of the parametric study on the drag coefficient. Again, variation in Strouhal number offer the greatest variation in drag, when compared to the effects of the Reynolds number. Peak thrust (represented as negative drag) was generated at $St = 0.4$ and occurred early in the downstroke. Conversely, the peak drag was

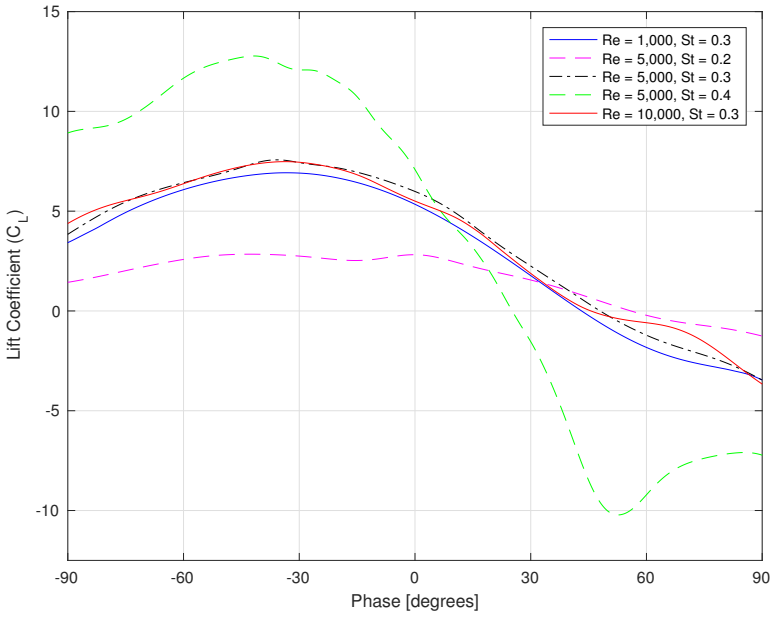

Figure 3.10: Coefficient of lift comparison with varying Reynolds and Strouhal numbers.

observed at the beginning and end of the downstroke for the $Re = 1,000$ and $St = 0.3$ case. In all the cases of the parametric study, peak drag was observed at the beginning and end of the downstroke where the airfoil was stationary. Therefore, it is observed that a LEV provides thrust despite the airfoil's motion being perpendicular. The effects of varying the Reynolds number are minimal, similar magnitudes were seen through the downstroke with a slightly negative phase shift observed with increasing Reynolds numbers.

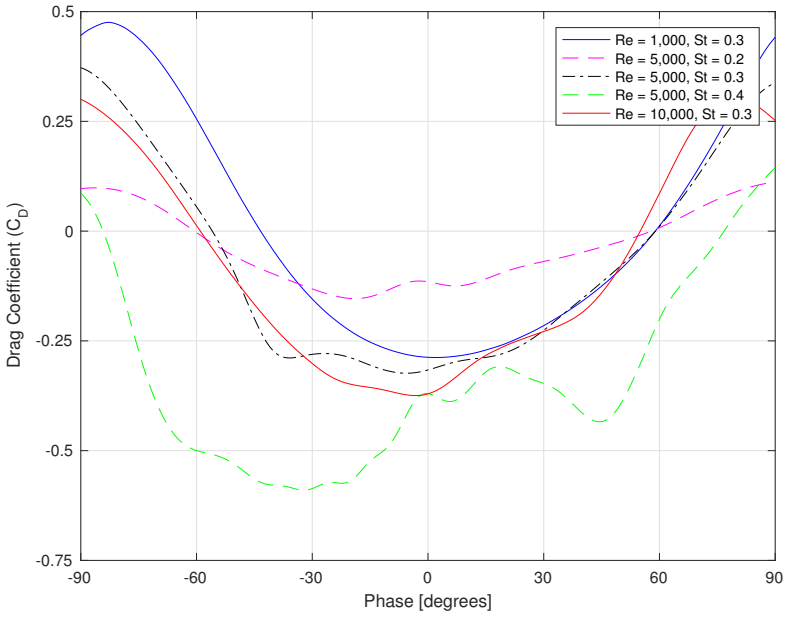

Figure 3.11: Coefficient of drag comparison with varying Reynolds and Strouhal numbers.

3.4.2 Parametric Study: Vortex Evolution

As a qualitative comparison, the LEV evolution is compared for the varying Reynolds numbers and Strouhal numbers in Figures 3.12 and 3.13, respectively. Each of these figures contains sub-figures of vorticity contours at regular phase increments of the plate's downstroke. Figures 3.12 illustrates the effects of Reynolds number on the evolution of the boundary layer and LEV formation. As expected, increased diffusion of vorticity into the freestream is seen at low Reynolds numbers, whereas the higher Reynolds number flows of 5,000 and 10,000 show sharp vortex edges. Overall, the evolution of the LEV during the downstroke is not highly dependent on the

Reynolds number, the location and size of the LEV is similar among all three varying Reynolds numbers and would justify the similar force data seen in Figures 3.10 and 3.11.

Alternatively, the effects of varying the Strouhal number are seen to have a large impact on the development of the LEV. Figure 3.13 compares the vorticity fields for $St = 0.2$, $St = 0.3$, and $St = 0.4$, for phases $-90°$ to $90°$ during the downstroke. At $St = 0.2$, the LEV develops at a similar rate to the $St = 0.3$ case; but at $St = 0.4$, the LEV develops quickly during the downstroke and entrains significant vorticity from the opposite side of the airfoil that has rolled around the leading edge. This entrained vorticity is opposite-signed to the LEV and begins a chaotic interaction with the LEV formation that results in an poorly defined vortex structure. Eslam Panah and Buchholz [7] observed similar behavior in their experimental results, where the LEV formation occurred earlier in the downstroke and also saw some LEVs being ejected normal to the airfoil surface. Alternatively, as discussed previously, the LEV at $St = 0.3$ has time to develop during the downstroke without interactions with shed vortices. Therefore, Figure 3.13 demonstrates the significance of $St = 0.3$ for a plunging airfoil and is consistent with prior studies which found that the optimal propulsion of biological specimens was achieved in the following Strouhal ranges: $0.25 < St < 0.35$ [30, 29].

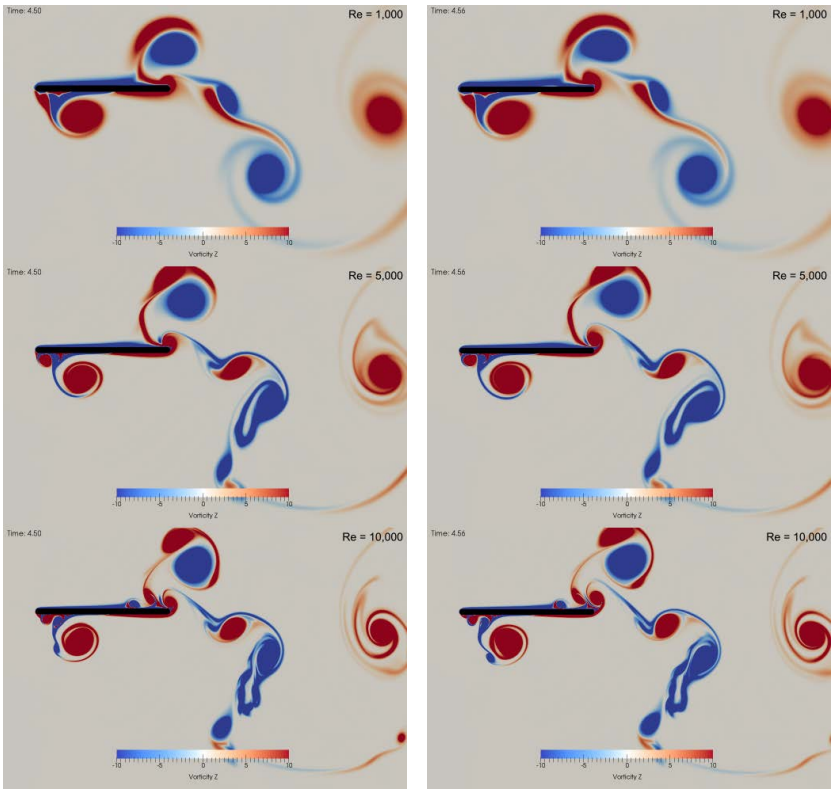

(a) $-90°$ (b) $-80°$

(c) $-70°$ (d) $-60°$

Figure 3.12: Cycle 2 phase synced vortex evolution at varying Reynolds numbers.

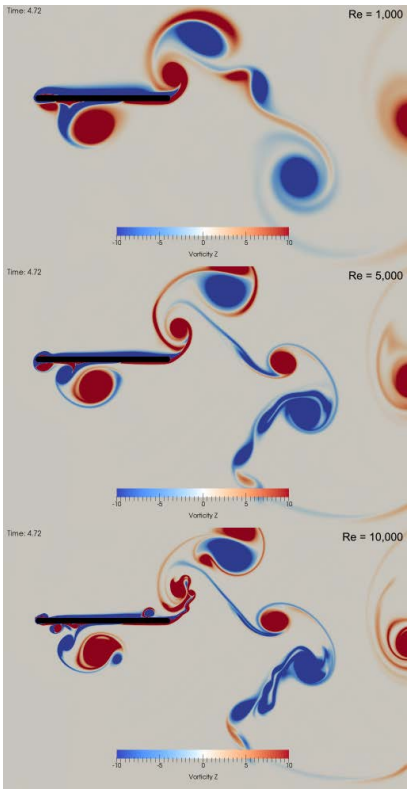

(e) $-50°$

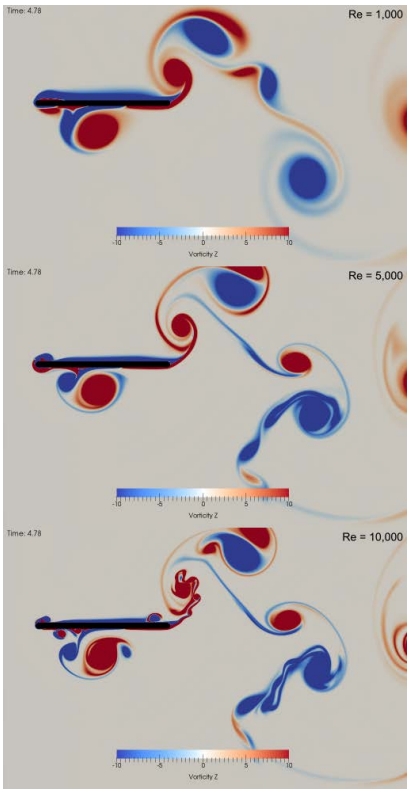

(f) $-40°$

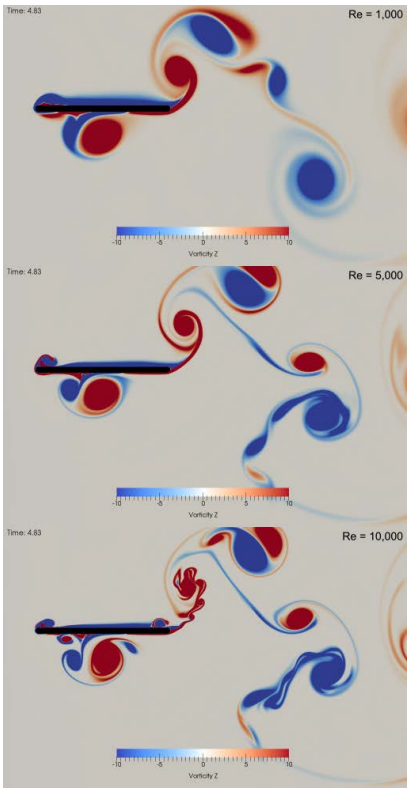

(g) $30°$

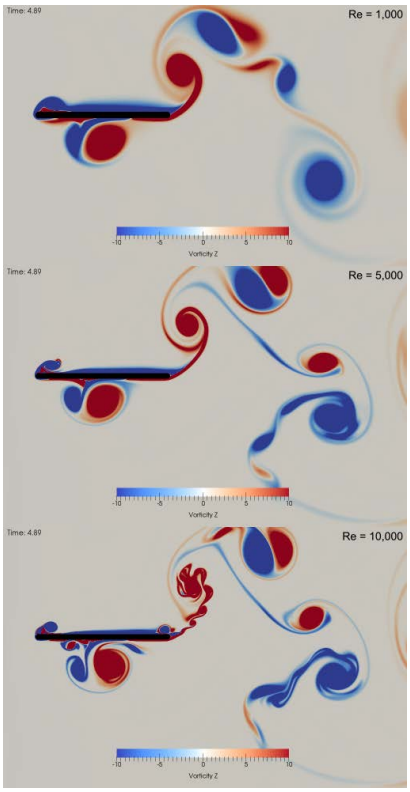

(h) $-20°$

Figure 3.12: Cycle 2 phase synced vortex evolution at varying Reynolds numbers.

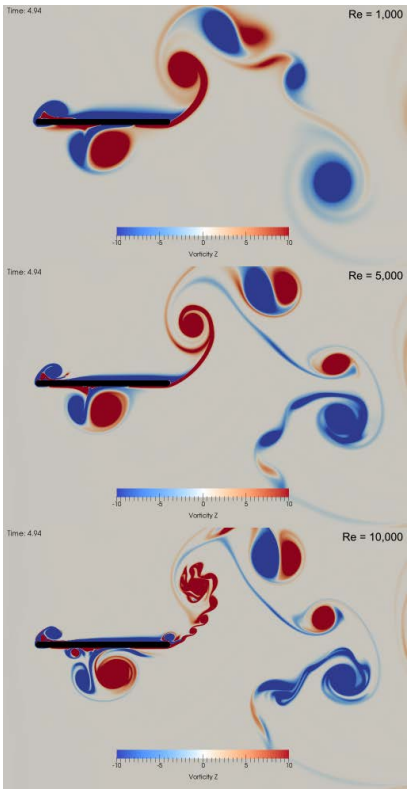

(i) $-10°$

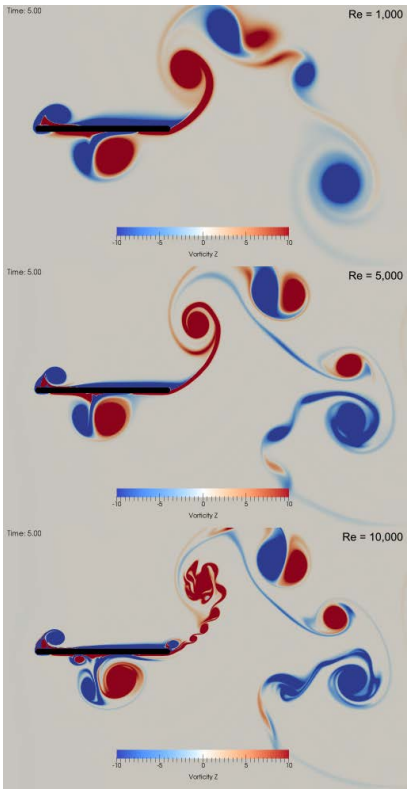

(j) $0°$

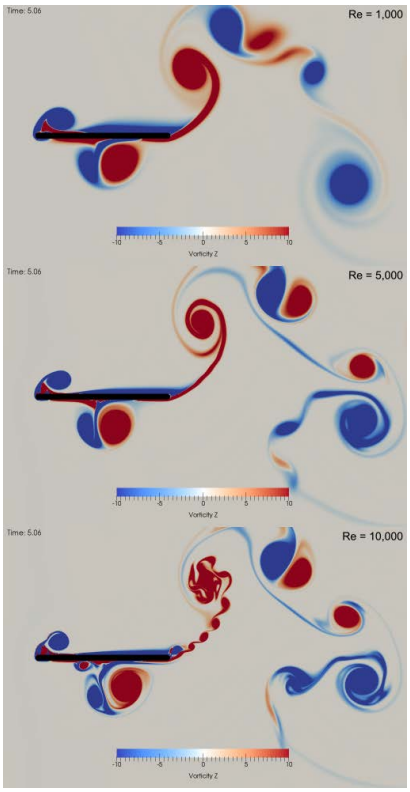

(k) $10°$

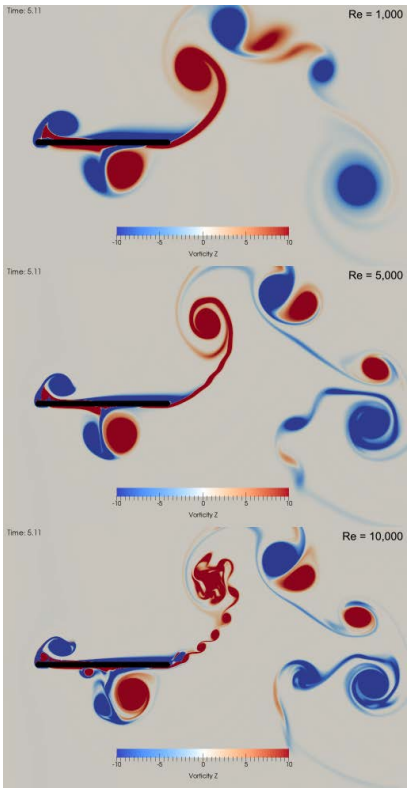

(l) $20°$

Figure 3.12: Cycle 2 phase synced vortex evolution at varying Reynolds numbers.

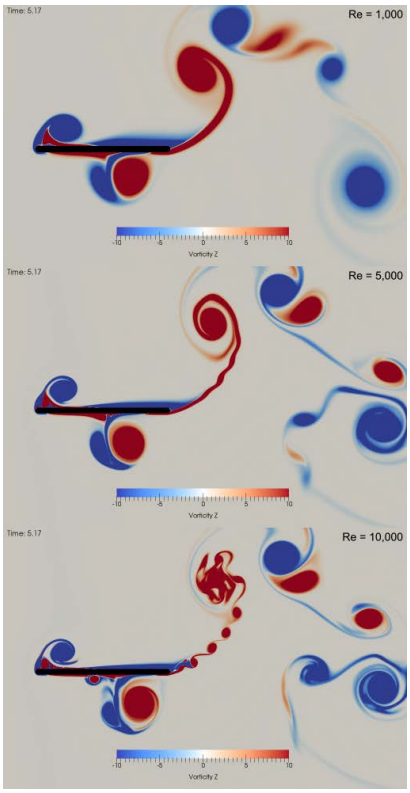

(m) 30°

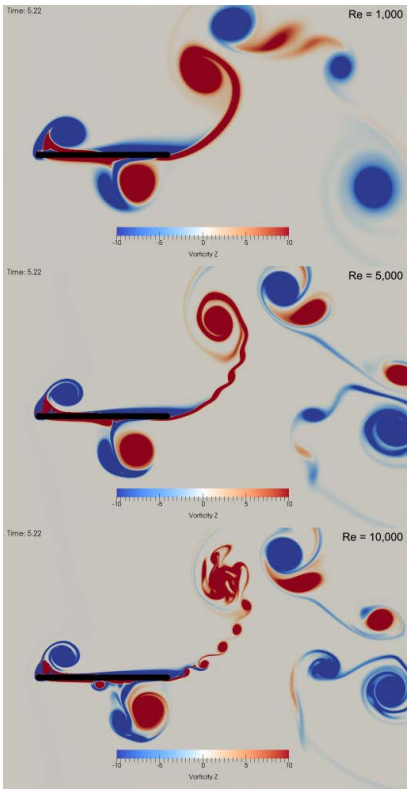

(n) 40°

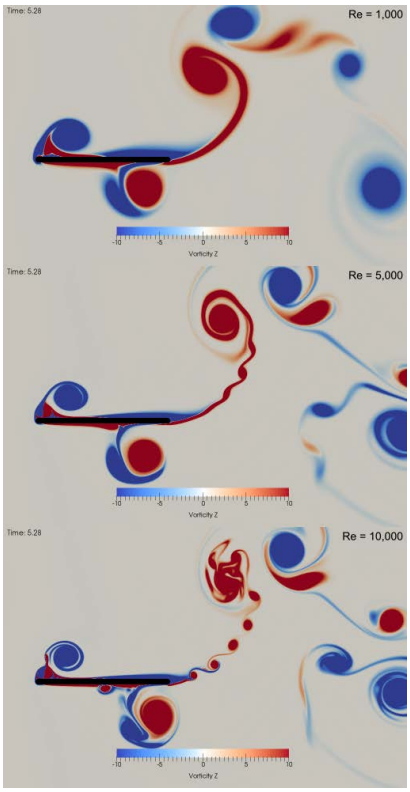

(o) 50°

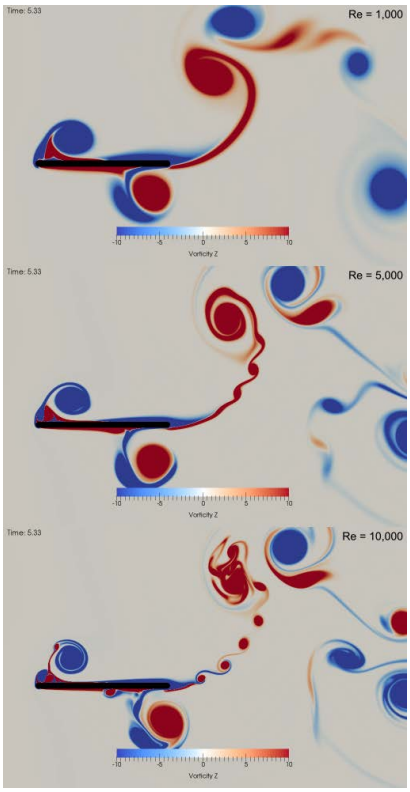

(p) 60°

Figure 3.12: Cycle 2 phase synced vortex evolution at varying Reynolds numbers.

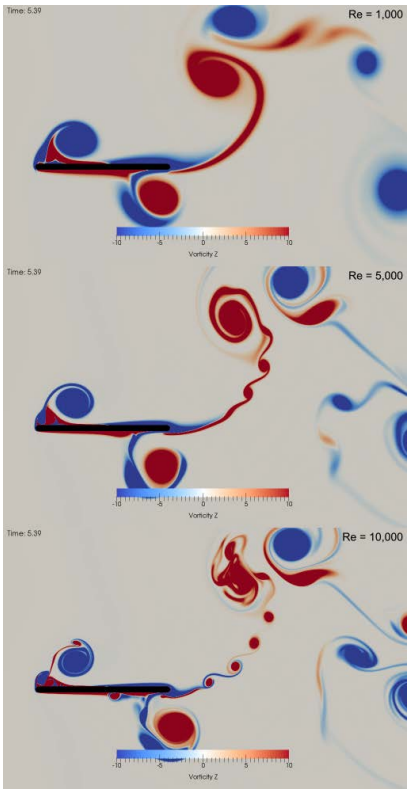

(q) 70°

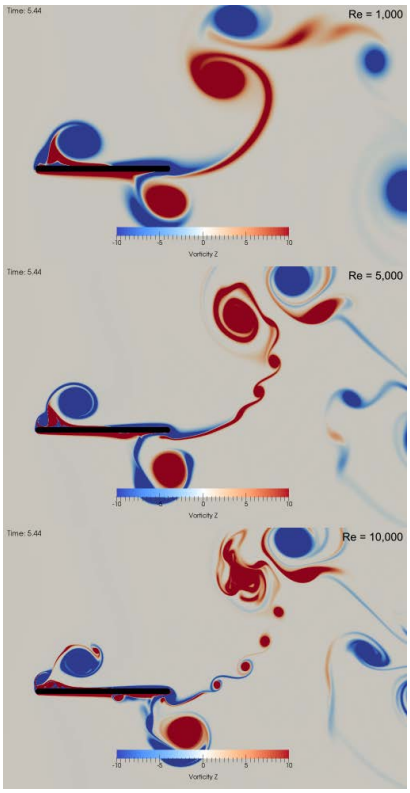

(r) 80°

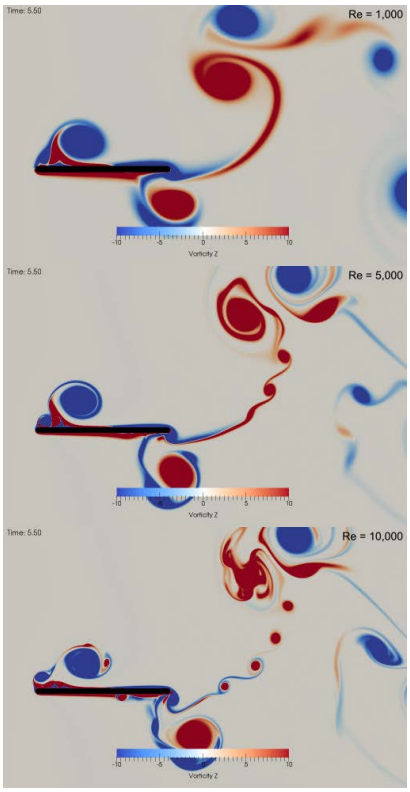

(s) 90°

Figure 3.12: Cycle 2 phase synced vortex evolution at varying Reynolds numbers.

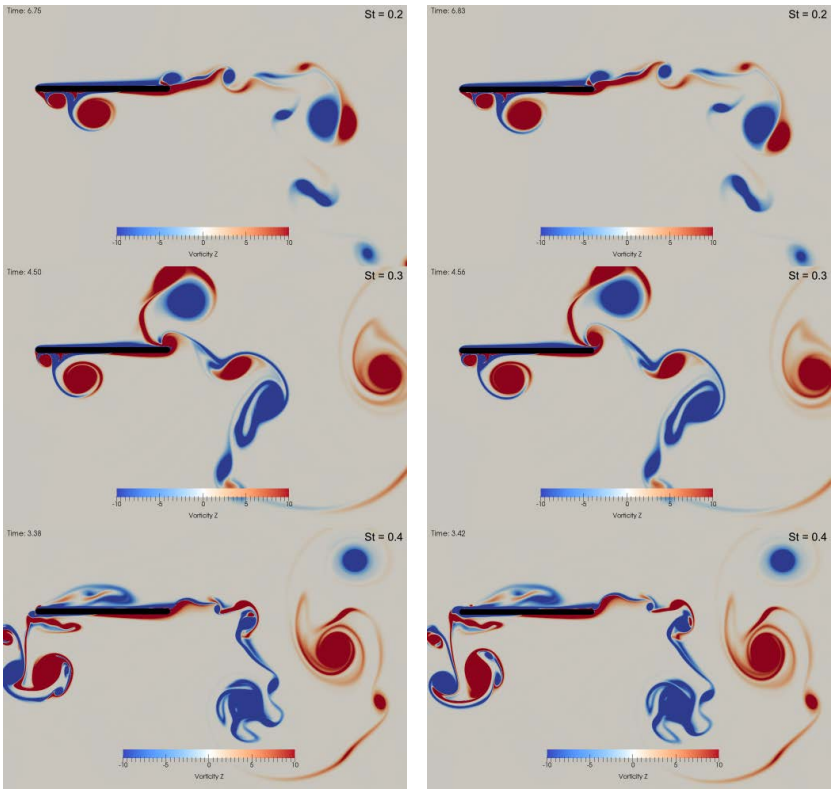

(a) $-90°$ (b) $-80°$

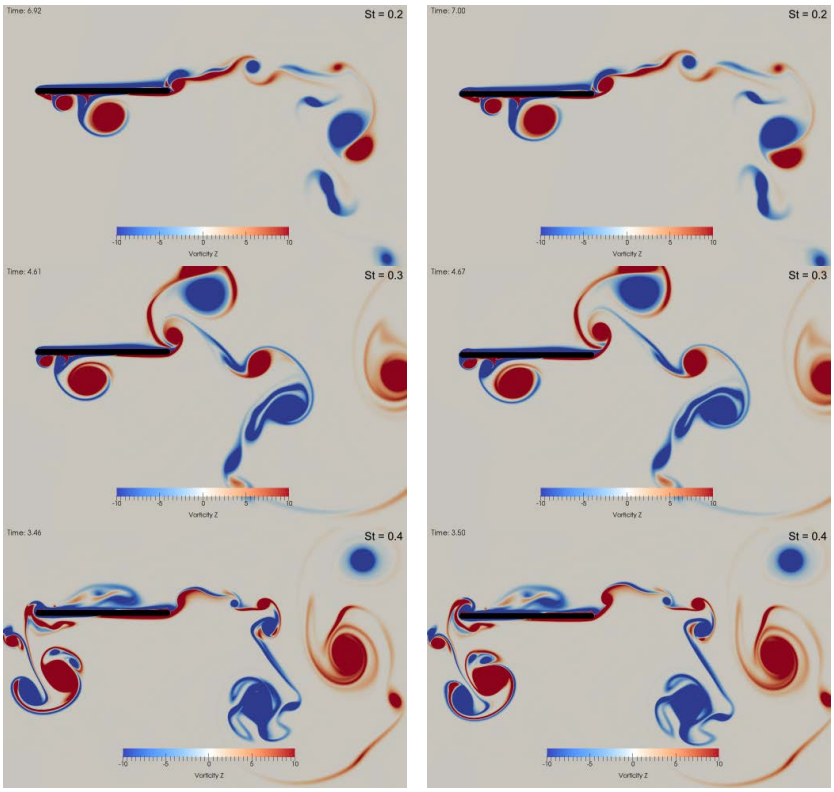

(c) $-70°$ (d) $-60°$

Figure 3.13: Cycle 2 phase synced vortex evolution at varying Strouhal numbers.

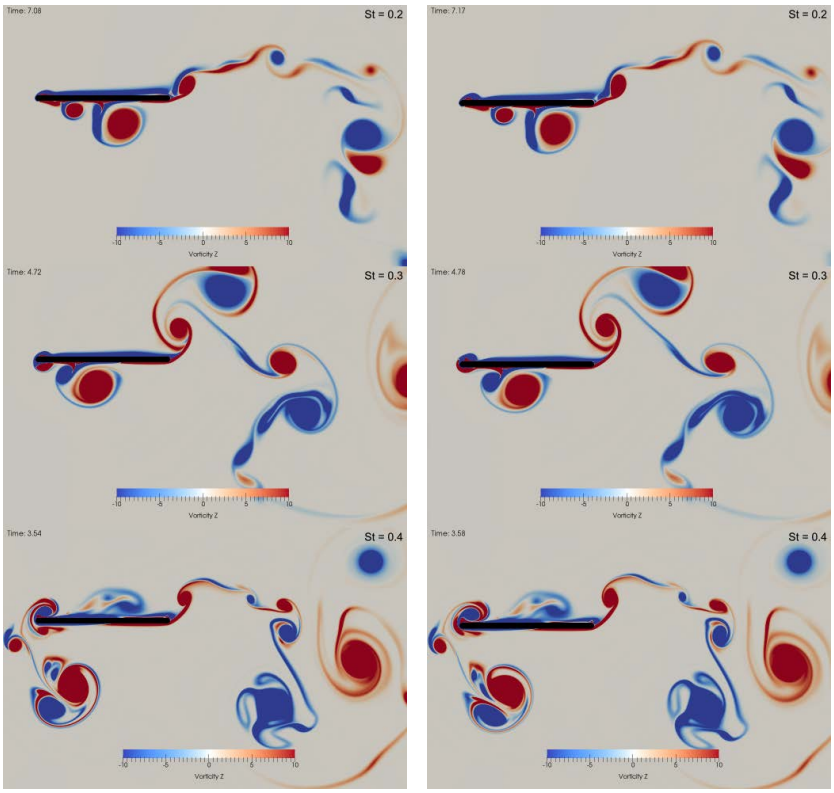

(e) $-50°$ (f) $-40°$

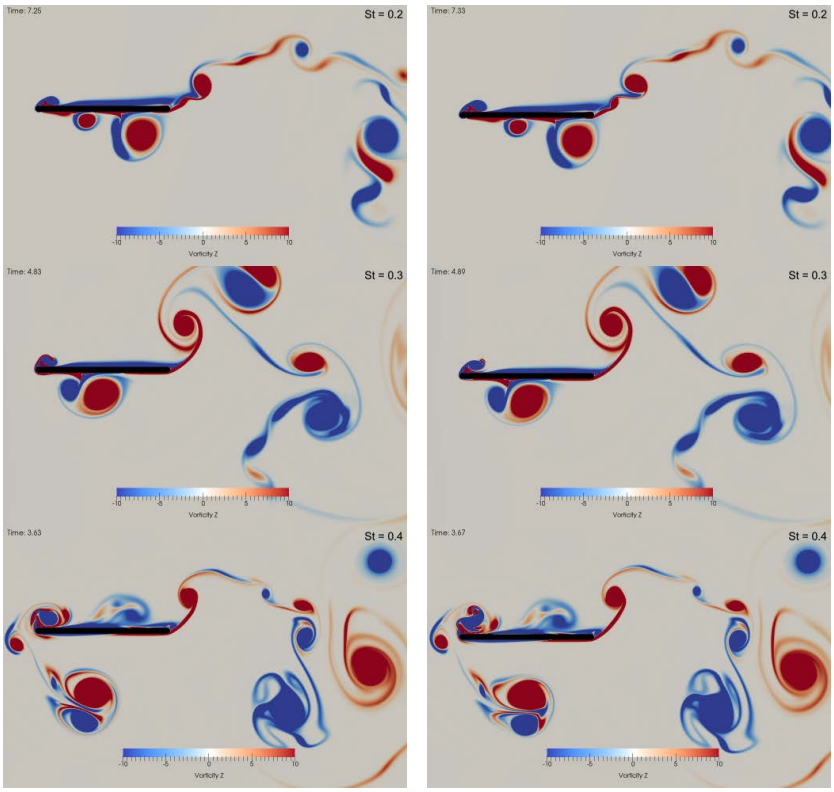

(g) $-30°$ (h) $-20°$

Figure 3.13: Cycle 2 phase synced vortex evolution at varying Strouhal numbers.

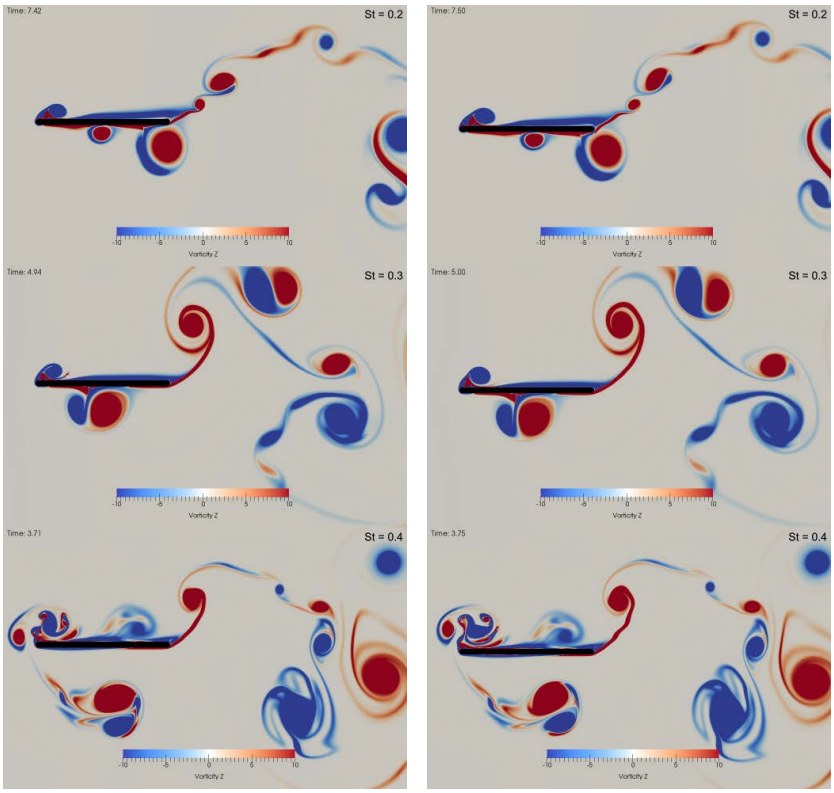

(i) $-10°$ (j) $0°$

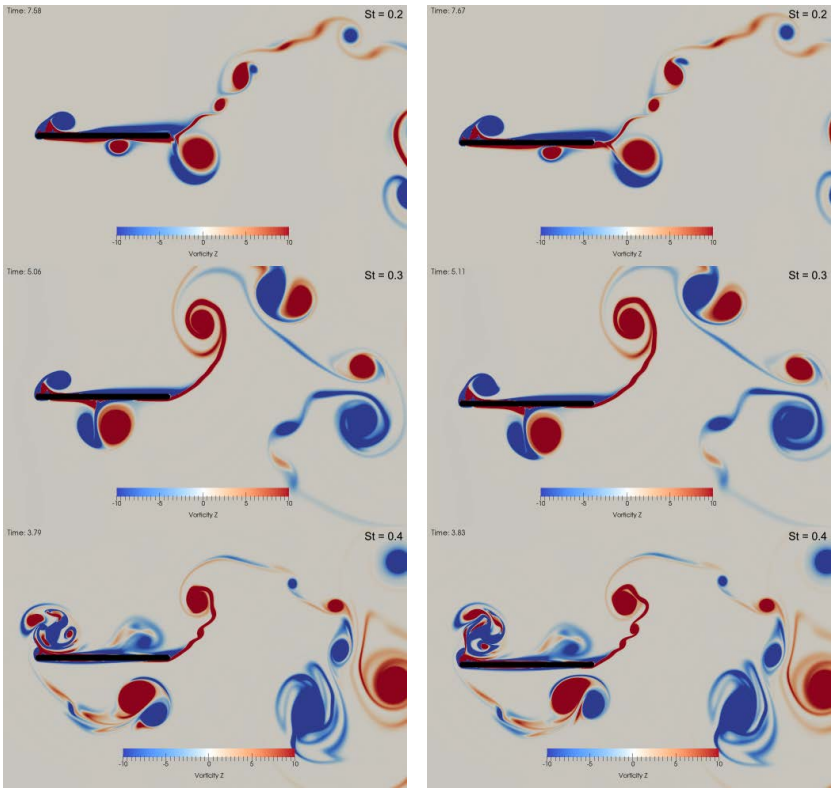

(k) $10°$ (l) $20°$

Figure 3.13: Cycle 2 phase synced vortex evolution at varying Strouhal numbers.

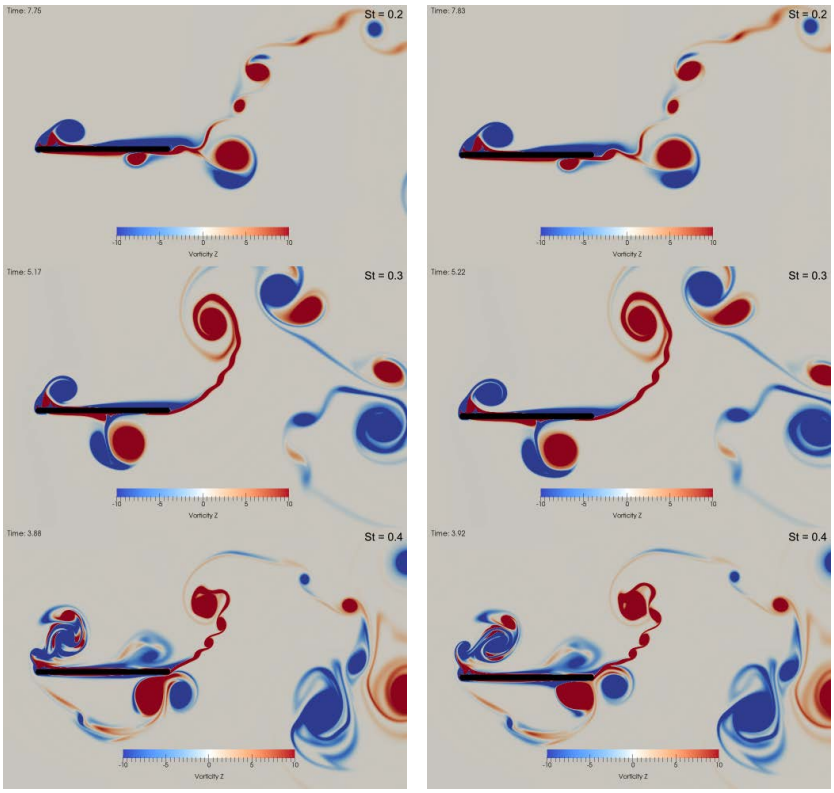

(m) 30° (n) 40°

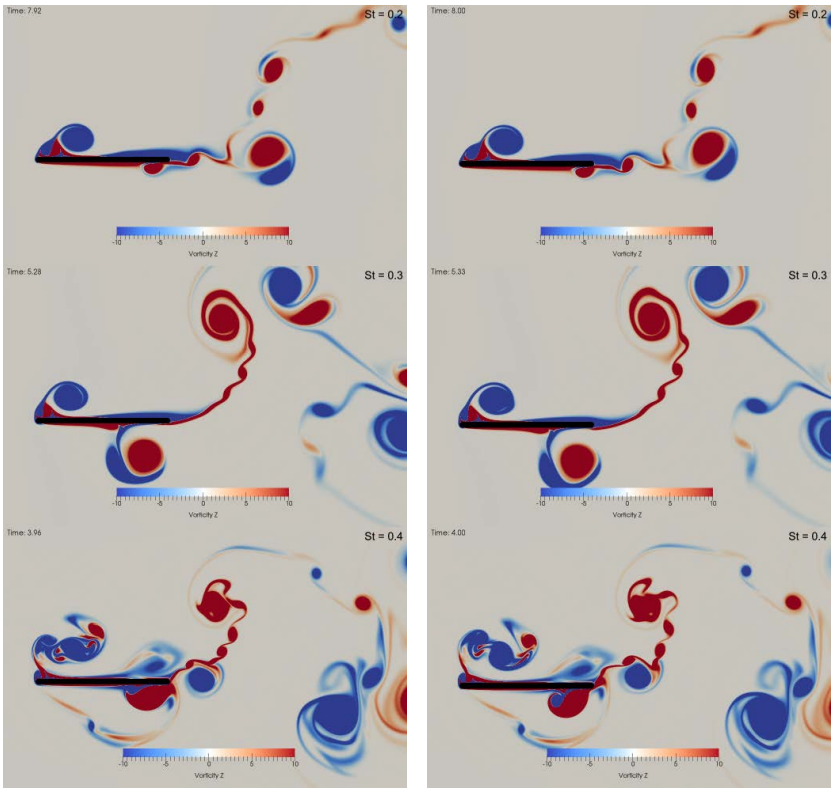

(o) 50° (p) 60°

Figure 3.13: Cycle 2 phase synced vortex evolution at varying Strouhal numbers.

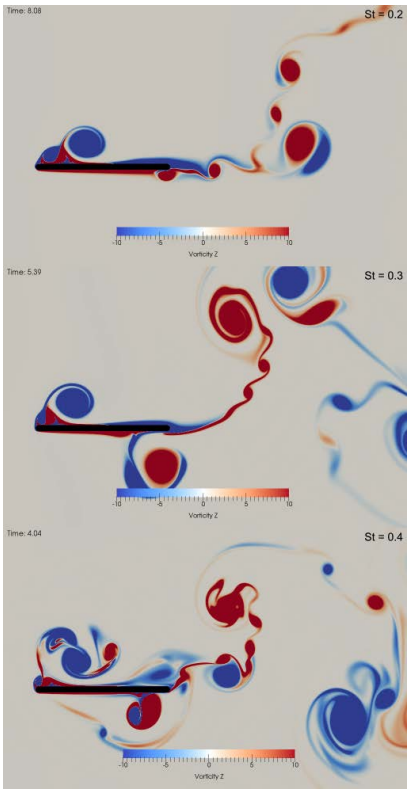

(q) 70°

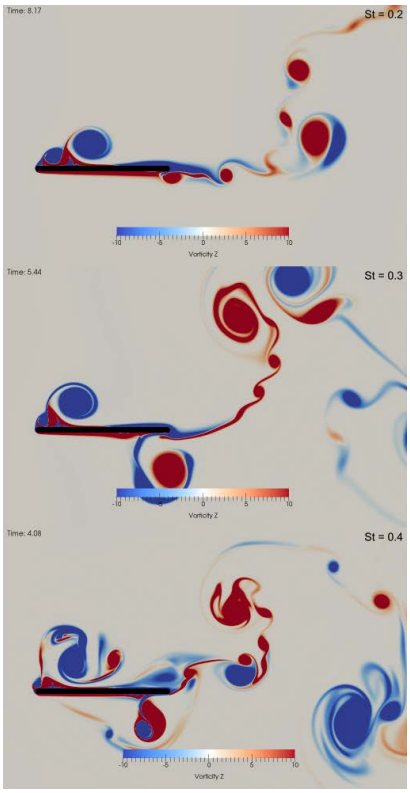

(r) 80°

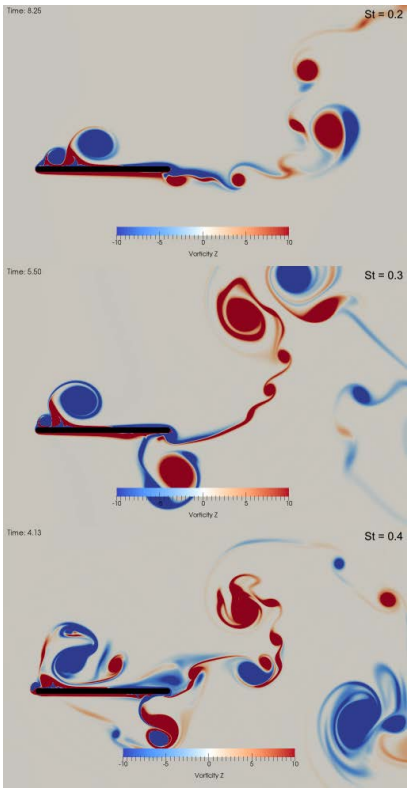

(s) 90°

Figure 3.13: Cycle 2 phase synced vortex evolution at varying Strouhal numbers.

3.4.3 Parametric Study: Vorticity Flux Analysis

Detailed vorticity flux analyses were conducted on the simulations of the parametric study using methods similar to Section 3.3. Figures 3.14, 3.15, 3.16, and 3.17 correspond to cases 1, 2, 3, and 4 of Table 3.2, respectively. The vorticity flux analysis for case 5 can be found in Section 3.3, where the simulation flux analysis was compared to the experimental data. Each figure shows the isolated vorticity fluxes during the plunging downstrokes of cycles 2-5 and were used to characterize the flow field and determine the validity of performing a two-dimensional simulation at thsse parameters.

It was shown in Section 3.3, that the two-dimensional simulation results yielded overall circulation and vorticity fluxes in good agreement with experimental results. Additionally, it was concluded that the deviations from the experimental data in later plunging cycles resulted from the lack of vortex breakdown which caused irregular vortex interactions and fluxes of vorticity that altered the evolution of the LEV.

Figure 3.14 shows the analysis for case 1 with $Re = 1,000$ and $St = 0.3$. All four plunging cycles show similar trends when comparing the isolated fluxes. This was not seen in the analysis of case 5, the highest Reynolds number looked at, $Re = 10,000$. The similarity of the vorticity flux analysis can be attributed to the formation of the LEVs occurring in the absence of lingering vortices. The vorticity fluxes show similar trends between cases 1 and 5, where the strength of the diffusive flux is approximately half the shear layer flux and the fluxes through s_2 and s_4 are minimal. Case 1 does show that the shear and diffusive fluxes have a wider region of peak flux,

the flux strength first builds during the initial 60° of the downstroke and then the next 60° exhibit peak flux before diminishing at the end of the downstroke. Case 5 showed longer periods of increasing flux (60°-70°) and a narrower region of peak flux (5°-10°). Additionally, when comparing the magnitudes of the total vorticity flux, case 1 is two orders of magnitudes less than case 5. This decrease in the vorticity fluxes' magnitudes can be attributed to the following: 1.) a decrease in the dynamic pressure at the airfoil's surface as a result of the reduced Reynolds number and 2.) increased viscous diffusion of vorticity into the the surrounding fluid. Because all four cycles of case 1 exhibit similar vorticity fluxes, it is hypothesized that adequate breakdown of the shed vortices has occurred. This would suggest that the mechanisms of vortex breakdown at low Reynolds number are not dependent upon three-dimensional effects. Therefore, it is concluded that the two-dimensional simulation results of case 1 adequately model the flow field and that three-dimensional effects are not as important in governing vortex evolution when viscous effects dominate.

Figure 3.15 corresponds to case 2, with $Re = 5,000$ and $St = 0.2$. Again, all four plunging cycles show similar trends when comparing the isolated fluxes. For case 2, the Reynolds number has increased the dynamic pressure at the airfoil's surface but viscous diffusion has diminished. The combined effects result in increased magnitudes of the vorticity fluxes and total flux. As the diffusion of vorticity has less relevance at $Re = 5,000$, the consistency of the plunging cycles must be accounted for elsewhere. Instead, the decreased plunging frequency, associated with the smaller Strouhal number, has resulted in increased significance of the freestream velocity to

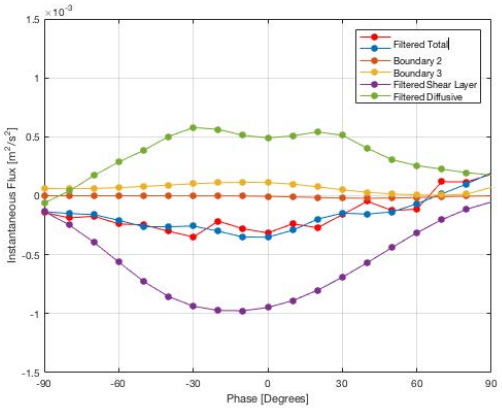

(a) Cycle 2

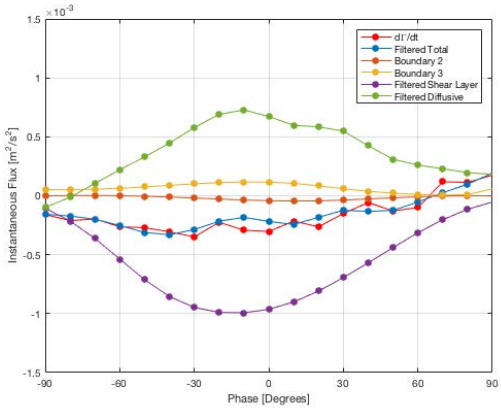

(b) Cycle 3

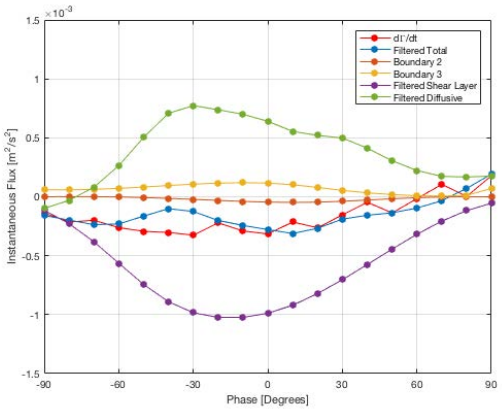

(c) Cycle 4

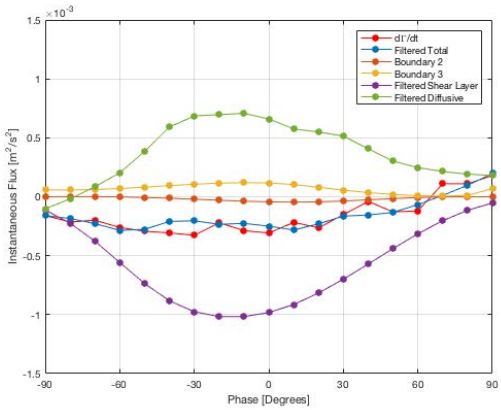

(d) Cycle 5

Figure 3.14: Vorticity flux analysis for Re = 1,000 and St = 0.3.

convect the LEV downstream. This is evident during the downstroke where there is a proportional increase in the vorticity flux through S_4, resulting from the mostly negative vorticity leaving the control region. Therefore, it is concluded that increased convection in the freestream direction at low Strouhal numbers acts to adequately remove prior cycle vortices. The nominal two-dimensional simulation of case 2 will not necessarily solve the breakdown of vortices but the formation of LEVs is unaffected due to the vortex convection downstream and accurately simulate the formation of an LEV.

Figure 3.16 shows the flux analysis for case 3 with $Re = 5,000$ and $St = 0.3$. In case 3, the Reynolds number is that same as case 2 but the Strouhal number is the same as case 1 and 5. Therefore, it is expected that the evolution of the LEV is in phase agreement with cases 1 and 5 but that the convection due to the reduced frequency, as seen in case 2, will be diminished in $St = 0.3$. Furthermore, at $Re = 5,000$ the diffusion of vorticity into the freestream, as seen in case 1, will be diminished as well. The net results of these effects is that the four plunging cycles begins to show variations in the vorticity fluxes, and in the shear layer flux specifically. Significant variations were also seen in case 5 for $Re = 10,000$ and $St = 0.3$, where it was concluded that the lack of three-dimensional effects in the two-dimensional simulation were inaccurately modeling the breakdown of the LEVs. It is reasonable to expect that the results of case 3 and 5 would be similar but that any physical deficiencies would be more prevalent at the higher Reynolds number where turbulent flow become prominent and three-dimensional structure are prevalent. In conclusion, the initial

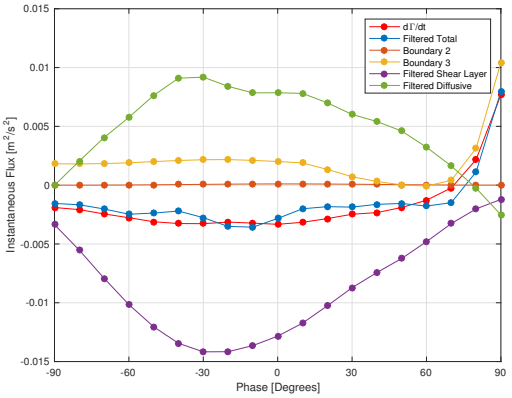

(a) Cycle 2

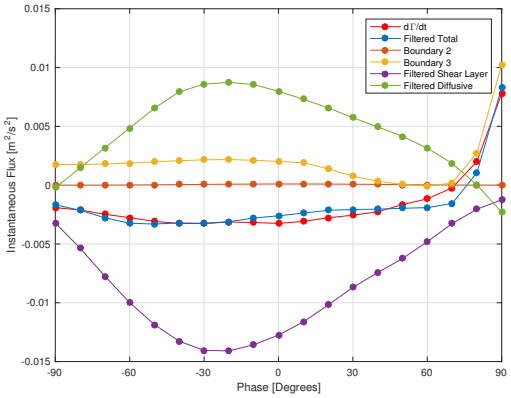

(b) Cycle 3

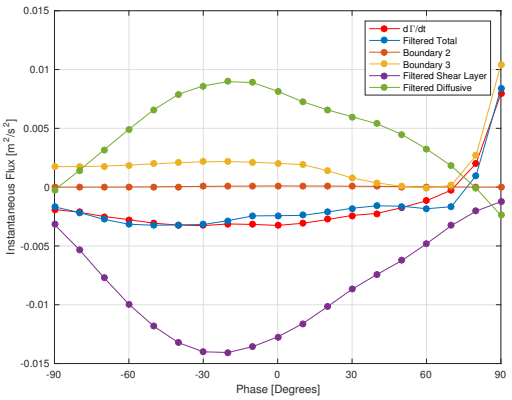

(c) Cycle 4

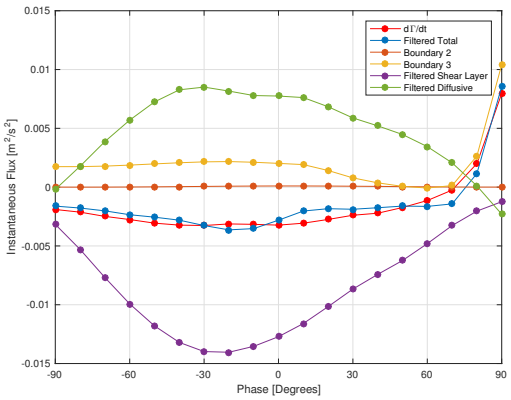

(d) Cycle 5

Figure 3.15: Vorticity flux analysis for Re = 5,000 and St = 0.2.

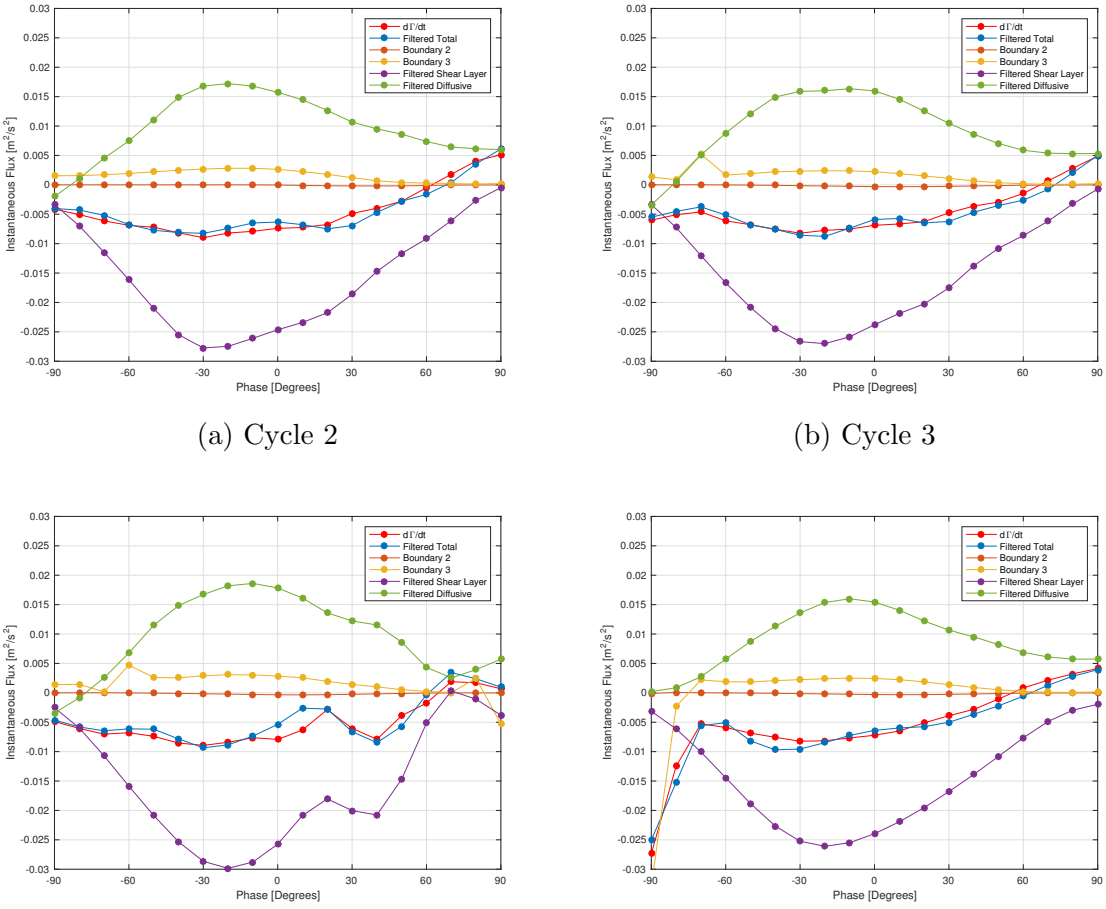

(a) Cycle 2

(b) Cycle 3

(c) Cycle 4

(d) Cycle 5

Figure 3.16: Vorticity flux analysis for Re = 5,000 and St = 0.3.

cycles of plunging motion for all cases should accurately simulate LEV formation in a two-dimensional simulation, but beyond that the lack of three-dimensional effects inaccurately model the vortex breakdown which affects LEV formation.

Lastly, Figure 3.17 shows the vorticity flux analysis for case 4 with $Re = 5,000$ and $St = 0.4$. Only one cycle of this case is needed to demonstrate that the simulations are not providing insightful analysis. As was seen in Figure 3.13, the

LEV formation coincides with significant amounts of opposite-signed vorticity being sucked around the leading edge. The vorticity from the opposite side of the airfoil is then entrained into the forming LEV. The net result is that the magnitudes of the vorticity fluxes in case 4 are diminished when compared to case 5. Furthermore, Figure 3.13 also shows that the LEV does not significantly convect downstream and is actually seen moving upstream and upward in later plunging cycles (not shown). As previously discussed in Section 3.4.2, this behavior is consistent with what was seen by Eslam Panah and Buchholz [7]. The pathway of the LEV can partly be attributed to the high Strouhal number where the plunging motion is the dominate motion over the freestream velocity and thus the LEV convects downstream very slowly. The additional directions of LEV trajectory in case 4, present the problem of using a control region that is ill fitted for the flow dynamics. As the control region was originally defined for case 5, it was determined that it was not suited for the irregular flow field of case 4. Therefore, any conclusions from case 4 were difficult to make and it is only hypothesized that the increased vortex interactions would result in additional three-dimensional structures that would not be correctly modeled with two-dimensional simulations.

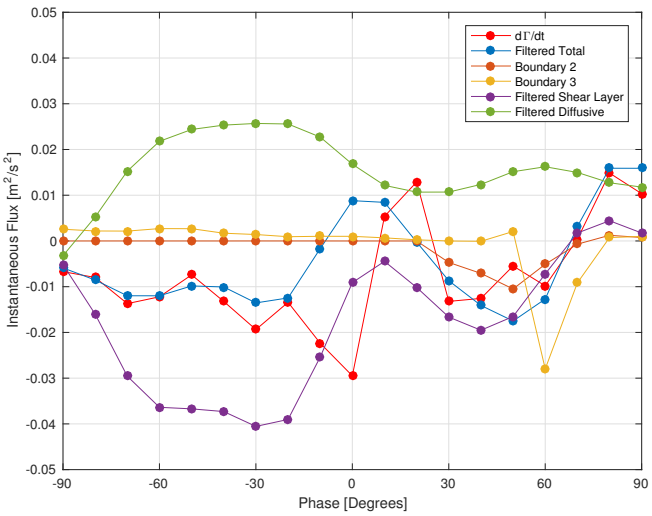

Figure 3.17: Representative vorticity flux analysis for Re = 5,000 and St = 0.4.

CHAPTER 4
CONCLUSIONS AND FUTURE WORK

4.1 Conclusions

This thesis developed a numerical framework for performing and analyzing two-dimensional unsteady flow simulations with a plunging airfoil. Elimination of the three-dimensional flow physics, through the use of two-dimensional simulations, allowed the investigation into the effects of three-dimensional flow physics by comparing the two-dimensional simulation to experimental results (inherent with three-dimensional physics). Interestingly, it was found that the absence of three-dimensional flow did not significantly alter global effects (i.e. lift and drag coefficients) on the airfoil despite deviations seen in the vortex evolution and transport of vorticity.

The base simulation case, $Re = 10,000$ and $St = 0.3$, was compared to experimental data for validation. Through the validation it was found that the lift and drag coefficients corresponded well between the filtered simulation and experimental data. The analysis of the simulation force data did present one of the shortcomings with the Ghost Fluid Method (GFM), where high frequency oscillations in the solution variables were seen around the moving boundary due to ghost cells transforming to fluid cells with no prior variable data. The oscillating force artifacts were easily compensated for through the use filtering because data the output was at high sampling rate (every iteration). For flow variables not output at each iteration, filtering was less accurate. Overlays of experimental and simulation vorticity contours validated that the

simulation could accurately model the LEV position and entrainment of secondary vorticity. But, despite secondary vorticity being entrained into the primary vortex, it is hypothesized that the lack of LEV breakdown in the simulations is in part due to the entrained secondary vorticity's inability to annihilate the primary vorticity. Presumably, the lack of three-dimensional mixing limits the vorticity annihilation. Lastly, the vorticity flux analysis provided insight into LEV formation for the base simulation. As the simulation progressed, the shed LEVs introduced increasingly irregular fluxes of vorticity that began to alter the formation of an LEV. Therefore, three-dimensional physics play a key role in the break down the vortices and suggest that the vorticity mixing and annihilation occur in the spanwise direction.

The parametric study provided insight into the effects of Reynolds and Strouhal numbers. It was seen that the Strouhal number has the greatest effect on both the lift and drag coefficients. The Reynolds number provided a slight phase shifting of the lift and drag forces, consistent with [9], but overall the magnitudes were similar. Utilizing both the vortex evolution and vorticity transport analyses, it was seen that the Strouhal number had a profound effect on the generation and interaction of LEVs, and the results were consistent with [7]. It was found that the greatest fluxes of vorticity were achieved at $St = 0.3$ and reinforced the significance of flapping motion in the following Strouhal ranges: $0.25 < St < 0.35$. The vorticity flux analysis provided insight into other flow mechanisms that offset the lack of three-dimensional physics on LEV formation, such as viscous diffusion in low Reynolds number cases and increased freestream convection.

4.2 Future Work

This thesis work has been in support of the vortex dynamics research conducted by Professor Buchholz's lab. Future work using simulations to study vortex dynamics has been shown to be feasible, even with the absence of three-dimensional flow. To fully realize the potential of DNS simulations and model the three-dimensional physics using the research code pELAFINT3D, it would require several hundred processor cores and several weeks to obtain a solution; the two-dimensional simulation at $Re = 10,000$ and $St = 0.3$ required 64 processors to obtain a solution in approximately two weeks. It is recommended that future work be conducted using this framework and be output at a frequency greater than 10° of airfoil motion during periods of key LEV formation; this will allow more accurate filtering of the solution data at the moving boundary. Increased dimensions of the domain and a higher frequency of outputting data will require several terabytes of storage space; the current two-dimensional simulations required approximately 300 gigabytes each. Additionally, the current serial flux analysis would require several days of processing using a single core. Therefore, to reduce the flux analysis processing time, parallelization of the code or integrating it into the pELAFINT3D libraries would reduce the computational analysis cost. In the end, the logical next step is to simulate in a three-dimensional domain and analyze the resulting flow field with greater fidelity than can be achieved with PIV.

APPENDIX
DERIVATIONS

This Appendix provides a detailed derivation of the equations used in the methods of Chapter 2.

A.1 Vorticity Flux Analysis

The vorticity flux analysis is derived from the vorticity transport equation, Equation A.1, where ν is a constant:

$$\frac{\partial \vec{\omega}}{\partial t} = (\vec{\omega} \cdot \nabla)\,\vec{u} - (\vec{u} \cdot \nabla)\,\vec{\omega} + \nu \nabla^2 \vec{\omega} \tag{A.1}$$

Because the simulations were conducted in a 2D domain, only the z-component of the vorticity is relevant and Equation A.1 can expanded for ω_z as follows:

$$\begin{aligned} \frac{\partial \omega_z}{\partial t} = &\left(\omega_x \frac{\partial u_z}{\partial x} + \omega_y \frac{\partial u_z}{\partial y} + \omega_z \frac{\partial u_z}{\partial z}\right) - \left(u_x \frac{\partial \omega_z}{\partial x} + u_y \frac{\partial \omega_z}{\partial y} + u_z \frac{\partial \omega_z}{\partial z}\right) \\ &+ \nu \left(\frac{\partial^2 \omega_z}{\partial x^2} + \frac{\partial^2 \omega_z}{\partial y^2} + \frac{\partial^2 \omega_z}{\partial z^2}\right) \end{aligned} \tag{A.2}$$

Additionally, several terms in Equation A.2 can be eliminated as three-dimensional mechanisms are not present in the 2D flow. Namely, Equations A.3, A.4, A.5, A.6, and A.7, contain derivatives with respect to z, the z-component of of velocity (u_z), or out of plane vorticity (ω_x and ω_y):

$$\cancel{\omega_x \frac{\partial u_z}{\partial x}} = 0 \tag{A.3}$$

$$\cancel{\omega_y \frac{\partial u_z}{\partial y}} = 0 \tag{A.4}$$

$$\omega_z \cancel{\frac{\partial u_z}{\partial z}} = 0 \tag{A.5}$$

$$\cancel{u_z \frac{\partial \omega_z}{\partial z}} = 0 \tag{A.6}$$

$$\cancel{\frac{\partial^2 \omega_z}{\partial z^2}} = 0 \tag{A.7}$$

Equation A.2 then becomes Equation A.8 but note that A.4 and A.7 have been retained as they will be used to alter the form of the equation for analysis:

$$\frac{\partial \omega_z}{\partial t} = \omega_z \frac{\partial u_z}{\partial z} - \left(u_x \frac{\partial \omega_z}{\partial x} + u_y \frac{\partial \omega_z}{\partial y} \right) + \nu \left(\frac{\partial^2 \omega_z}{\partial x^2} + \frac{\partial^2 \omega_z}{\partial y^2} + \frac{\partial^2 \omega_z}{\partial z^2} \right) \tag{A.8}$$

At this point it is necessary to alter Equation A.8 from viewing the vorticity in a differential element to viewing vorticity in a control region at the top surface of the plate. The control region was specified in Section 3 but for now will be defined as the in-plane area, dA_z, and is introduced in the integral form of Equation A.8 as Equation A.9:

$$\begin{aligned} \iint_{A_z} \frac{\partial \omega_z}{\partial t} \, dA_z = & \iint_{A_z} \left(\omega_z \frac{\partial u_z}{\partial z} - u_x \frac{\partial \omega_z}{\partial x} - u_y \frac{\partial \omega_z}{\partial y} \right) dA_z \\ & + \nu \iint_{A_z} \left(\frac{\partial^2 \omega_z}{\partial x^2} + \frac{\partial^2 \omega_z}{\partial y^2} + \frac{\partial^2 \omega_z}{\partial z^2} \right) dA_z \end{aligned} \tag{A.9}$$

The LHS of Equation A.9 can be adjusted as A.11 with the introduction of the definition of circulation given in Equation A.10. Equation A.11 is the time rate of change in circulation of the planar control region dA_z:

$$\vec{\Gamma} = \iint_{\vec{A}} (\nabla \times \vec{u}) \cdot d\vec{A} = \iint_{\vec{A}} \vec{\omega} \cdot d\vec{A} \Longrightarrow \Gamma_z = \iint_{A_z} \omega_z \, dA_z \tag{A.10}$$

$$\iint_{A_z} \frac{\partial \omega_z}{\partial t} \, dA_z = \frac{\partial}{\partial t} \left(\iint_{A_z} \omega_z \, dA_z \right) = \frac{\partial \Gamma_z}{\partial t} \tag{A.11}$$

The first term on the RHS of Equation A.9 is the convective flux of vorticity into the control region. Using the continuity equation for an incompressible flow,

Equation A.4 can be changed as shown in Equation A.12. Then first term on the RHS of Equation A.9 can be altered as shown in A.13:

$$\omega_z \frac{\partial u_z}{\partial z} = -\omega_z \left(\frac{\partial u_x}{\partial x} + \frac{\partial u_y}{\partial y} \right) \tag{A.12}$$

$$\begin{aligned} &\iint_{A_z} \left(\omega_z \frac{\partial u_z}{\partial z} - u_x \frac{\partial \omega_z}{\partial x} - u_y \frac{\partial \omega_z}{\partial y} \right) dA_z \\ &= \iint_{A_z} \left(-\omega_z \left(\frac{\partial u_x}{\partial x} + \frac{\partial u_y}{\partial y} \right) - u_x \frac{\partial \omega_z}{\partial x} - u_y \frac{\partial \omega_z}{\partial y} \right) dA_z \end{aligned} \tag{A.13}$$

Applying the Product Rule and then Green's Theorem to the RHS of Equation A.13, the form can be altered as shown in Equations A.14a, A.14b, and A.14c:

$$\begin{aligned} &\iint_{A_z} \left(-\omega_z \left(\frac{\partial u_x}{\partial x} + \frac{\partial u_y}{\partial y} \right) - u_x \frac{\partial \omega_z}{\partial x} - u_y \frac{\partial \omega_z}{\partial y} \right) dA_z \\ &= -\iint_{A_z} \left(\frac{\partial}{\partial x}(\omega_z u_x) + \frac{\partial}{\partial y}(\omega_z u_y) \right) dA_z \end{aligned} \tag{A.14a}$$

$$= -\oint_s \left((\omega_z u_y)\, dx + (\omega_z u_x)\, dy \right) \tag{A.14b}$$

$$= -\oint_s \omega_z (\vec{u} \cdot \hat{n})\, ds \tag{A.14c}$$

Where s is the boundary of the planar control region A_z and $\hat{n}$ is the boundary's planar normal which points outward from the control region. Equation A.14c can be interpreted as the flux of vorticity leaving the control region.

Finally, the last term in Equation A.9, the diffusion flux of vorticity within the control region, can be expressed as the change of pressure along the surface of the airfoil. To begin, the area integral is converted to a line integral as shown in Equation

A.15a through A.15c:

$$\nu \iint_{A_z} \left(\frac{\partial^2 \omega_z}{\partial x^2} + \frac{\partial^2 \omega_z}{\partial y^2} + \frac{\partial^2 \omega_z}{\partial z^2} \right) dA_z = \nu \iint_{A_z} \nabla^2 \omega_z \, dA_z \tag{A.15a}$$

$$= \nu \iint_{A_z} (\nabla \cdot \nabla \omega_z) \, dA_z \tag{A.15b}$$

$$= \nu \oint_{s} (\nabla \omega_z \cdot \hat{n}) \, ds \tag{A.15c}$$

Physcially, Equation A.15c is accounting for the diffusion flux of vorticity around the closed edge (s) containing the control region A_z. It can be assumed that the mechanisms of vorticity diffusion away from a surface are negligible [10, 3] and therefore Equation A.15c becomes a line integral along the surface of the control region:

$$\nu \oint_{s} (\nabla \omega_z \cdot \hat{n}) \, ds = \nu \int_{s_4} \frac{\partial \omega_z}{\partial \hat{n}} \, ds_4 \tag{A.16}$$

Being consistent with the vorticity flux analysis performed on the experimental PIV data given by Akkala [1], the vorticity gradient in Equation A.16 is transformed into the gradient of the pressure along the surface of the airfoil:

$$\nu \int_{s_4} \frac{\partial \omega_z}{\partial \hat{n}} \, ds_4 = \frac{1}{\rho} \int_{s_4} \frac{\partial p}{\partial x} \, ds_4 \tag{A.17}$$

This simplification is only possible because the control surface is along the flat portion of the airfoil and because the airfoil undergoes plunging motion soley in the y-direction.

Putting together all the changes, the final form of the flux analysis is given in Equation A.18:

$$\frac{\partial \Gamma_z}{\partial t} = - \oint_{s} \omega_z (\vec{u} \cdot \hat{n}) \, ds + \frac{1}{\rho} \int_{s_4} \frac{\partial p}{\partial x} \, ds_4 \tag{A.18}$$

REFERENCES

[1] J. M. Akkala. *Understanding and Controlling Vorticity Transport in Unsteady, Separated Flows*. PhD thesis, University of Iowa, 2015.

[2] Z. Carr, C. Chen, and M. J. Ringuette. The effect of aspect ratio on the three-dimensional vortex formation of rotating flat-plate wings. In *50th AIAA Aerospace Sciences Meeting including the New Horizons Forum and Aerospace Exposition*, Nashville, Tennessee, 9–12 January 2012. AIAA Paper 2012-912.

[3] B. Cheng, S. Sane, G. Barbera, D. Troolin, T. Strand, and X. Deng. Three-dimensional flow visualization and vorticity dynamics in revolving wings. *Expts. Fluids*, 54, 2013.

[4] J. Choi, T. Colonius, and D. R. Williams. Surging and plunging oscillations of an airfoil at low reynolds number. *J. Fluid Mech.*, 763:237–253, 2015.

[5] T. L. Doligalski, C. R. Smith, and J. D. A. Walker. Vortex interactions with walls. *Annu. Rev. Fluid Mech.*, 26:573–616, 1994.

[6] C. P. Ellington, C. van den Berg, A. P. Willmott, and A. L. R. Thomas. Leading-edge vortices in insect flight. *Nature*, 384:626–630, 1996.

[7] A. Eslam Panah and J. H. J. Buchholz. Parameter dependence of vortex interactions on a two-dimensional plunging plate. *Expts. Fluids*, 55(3):1687, 2014.

[8] P.W. Hammerton and E.J. Kerschen. Leading-edge receptivity for bodies with mean aerodynamic loading. *J. Fluid Mech.*, 535:1–32, 2005.

[9] A. R. Jones and H. Babinsky. Reynolds number effects on leading edge vortex development on a waving wing. *Expts. Fluids*, 51:197–210, 2011.

[10] D. Kim and M. Gharib. Flexibility effects on vortex formation of translating plates. *J. Fluid Mech.*, 677:255–271, 2011.

[11] M. M. Koochesfahani. Vortical patterns in the wake of an oscillating airfoil. *AIAA J.*, 27(9):1200–1205, 1989.

[12] G. C. Lewin and H. Haj-Hariri. Modelling thrust generation of a two-dimensional heaving airfoil in a viscous flow. *J. Fluid Mech.*, 492:339–362, 2003.

[13] K. B. Lua, T. T. Lim, K. S. Yeo, and G. Y. Oo. Wake-structure formation of a heaving two-dimensional elliptic airfoil. *AIAA J.*, 45(7):1571–1583, 2007.

[14] H. Luo et al. On the numerical oscillation of the direct-forcing immersed boundary method for moving boundaries. *Computers & Fluids*, 56:61–76, 2012.

[15] K. W. Mangler and J. H. B. Smith. A theory of the flow past a slender delta wing with leading edge separation. *P. Roy. Soc. Lond. A Mat.*, 251(1265):200–217, 1959.

[16] M. Milano and M. Gharib. Uncovering the physics of flapping flat plates with artificial evolution. *J. Fluid Mech.*, 534:403–409, 2005.

[17] F. Mohaghegh, John Mousel, and H.S Udaykumar. Comparison of sharp interface and smoothed profile methods for laminar flow analysis over stationary and moving boundaries. In *ASME 2014 4th Joint US-European Fluids Engineering Division Summer Meeting*, pages V01AT03A004–V01AT03A004, 2014.

[18] F. Mohaghegh and H.S. Udaykumar. Comparison of sharp and smoothed interface methods for simulation of particulate ows i: Fluid structure interaction for moderate reynolds numbers. *Computers & Fluids*, 140:39–58, 2016.

[19] F. Mohaghegh and H.S. Udaykumar. Comparison of sharp and smoothed interface methods for simulation of particulate flows ii: Inertial and added mass effects. *Computers & Fluids*, 143:103–119, 2017.

[20] J. A. Mousel. *A Massively Parallel Adaptive Sharp Interface Solver with Application to Mechanical Heart Valve Simulations*. PhD thesis, University of Iowa, 2012.

[21] F. T. Muijres, L. C. Johansson, R. Barfield, M. Wolf, G. R. Spedding, and A. Hedenstrom. Leading-edge vortex improves lift in slow-flying bats. *Science*, 319:1250–1253, 2008.

[22] A. Eslam Panah, J.M. Akkala, and J.H.J. Buchholz. Vorticity transport and the leading-edge vortex of a plunging airfoil. *Expts. Fluids*, 2015. in review.

[23] C. W. Pitt Ford and H. Babinsky. Lift and the leading edge vortex. In *50th AIAA Aerospace Sciences Meeting*, Nashville, TN, January 2012. AIAA Paper 2012-911.

[24] E. Polhamus. Application of the leading-edge-suction analogy of vortex lift to the drag due to lift of sharp-edge delta wings. Technical Report NASA TN D-4739, Langley Research Center, Hampton, VA, August 1968.

[25] D. Rival, T. Prangemeier, and C. Tropea. The influence of airfoil kinematics on the formation of leading-edge vortices in bio-inspired flight. *Expts. Fluids*, 46:823–833, 2009.

[26] D. E. Rival, J. Kriegseis, P. Schaub, A. Widmann, and C. Tropea. A criterion for vortex separation on unsteady aerodynamic profiles. In *51st AIAA Aerospace Sciences Meeting*, Grapevine, TX, 2013. AIAA. AIAA Paper 2013-0836.

[27] W. Shyy, P. Trizilla, C. k. Kang, and H. Aono. Can tip vortices enhance lift of a flapping wing? *AIAA J.*, 47(2):289–293, 2009.

[28] G. K. Taylor, R. L. Nudds, and A. L. R. Thomas. Flying and swimming animals cruise at a strouhal number tuned for high power efficiency. 425:707–711, 2003.

[29] G. S. Triantafyllou, M. S. Triantafyllou, and M. A. Grosenbaugh. Optimal thrust development in oscillating foils with application to fish propulsion. 7:205–224, 1993.

[30] M. S. Triantafyllou, G. S. Triantafyllou, and R. Gopalkrishnan. Wake mechanics for thrust generation in oscillating foils. 3(12):2835–2837, 1991.

[31] P. Trizila, C. K. Kang, H. Aono, W. Shyy, and M. Visbal. Low-reynolds-number aerodynamics of a flapping rigid flat plate. *AIAA J.*, 49:806–823, 2011.

[32] L.L. van Dommelen and S.F. Shen. The spontaneous generation of the singularity in a separating laminar boundary layer. *J. Comp. Phys.*, 38:125–140, 1980.

[33] M. R. Visbal. High-fidelity simulation of transitional flows past a plunging airfoil. *AIAA J.*, 47(11):2685–2697, 2009.

[34] D. R. Warrick, B. W. Tobalske, and D. R. Powers. Lift production in the hovering hummingbird. *Proc. R. Soc. B*, 276:3747–3752, 2009.

[35] C. J. Wojcik and J. H. J. Buchholz. Vorticity transport in the leading-edge vortex on a rotating blade. *J. Fluid Mech.*, 743:249–261, 2014.